CORA Cork Open Research Archive
Cartlann Taighde Oscailte Chorcaí

Title	Water-wave interaction with submerged porous elastic disks
Authors	Zheng, S.;Meylan, M. H.;Greaves, D.;Iglesias, Gregorio
Publication date	2020-04-17
Original Citation	Zheng, S., Meylan, M. H., Greaves, D. and Iglesias, G. (2020) 'Water-wave interaction with submerged porous elastic disks', Physics of Fluids, 32(4), 047106 (20pp). https://doi.org/10.1063/5.0006119
Type of publication	Article (peer-reviewed)
Link to publisher's version	https://aip.scitation.org/doi/10.1063/5.0006119 - 10.1063/5.0006119
Rights	© 2020, the Authors. Published under license by AIP Publishing. This article may be downloaded for personal use only. Any other use requires prior permission of the author and AIP Publishing. This article appeared as: Zheng, S., Meylan, M. H., Greaves, D. and Iglesias, G. (2020) 'Water-wave interaction with submerged porous elastic disks', Physics of Fluids, 32(4), 047106 (20pp), doi: 10.1063/5.0006119, and may be found at https://doi.org/10.1063/5.0006119
Download date	2026-11-15 18:16:50
Item downloaded from	https://hdl.handle.net/10468/9843

UCC
University College Cork, Ireland
Coláiste na hOllscoile Corcaigh

Physics of Fluids

Water-wave interaction with submerged porous elastic disks

Cite as: Phys. Fluids **32**, 047106 (2020); https://doi.org/10.1063/5.0006119
Submitted: 27 February 2020 . Accepted: 01 April 2020 . Published Online: 17 April 2020

S. Zheng (郑思明), M. H. Meylan, D. Greaves, and G. Iglesias

View Online Export Citation CrossMark

ARTICLES YOU MAY BE INTERESTED IN

Effects of the fresh mixture temperature on thermoacoustic instabilities in a lean premixed swirl-stabilized combustor
Physics of Fluids **32**, 047101 (2020); https://doi.org/10.1063/1.5133859

Dynamics of coherent structures in turbulent square duct flow
Physics of Fluids **32**, 045106 (2020); https://doi.org/10.1063/5.0001977

Papers from the 2019 Institute of Non-Newtonian Fluid Mechanics Meeting in Lake Vyrnwy, Wales
Physics of Fluids **32**, 040401 (2020); https://doi.org/10.1063/5.0008256



AIP Publishing

© 2020 Author(s).

Physics of Fluids ARTICLE scitation.org/journal/phf

Water-wave interaction with submerged porous elastic disks

Cite as: Phys. Fluids 32, 047106 (2020); doi: 10.1063/5.0006119
Submitted: 27 February 2020 • Accepted: 1 April 2020 •
Published Online: 17 April 2020

View Online Export Citation CrossMark

S. Zheng (郑思明),[1,2,a)] M. H. Meylan,[3] D. Greaves,[2] and G. Iglesias[2,4]

AFFILIATIONS

[1]State Key Laboratory of Hydraulic Engineering Simulation and Safety, Tianjin University, Tianjin 300072, China
[2]School of Engineering, Computing and Mathematics, University of Plymouth, Drake Circus, Plymouth PL4 8AA, United Kingdom
[3]School of Mathematical and Physical Sciences, The University of Newcastle, Callaghan 2308, Australia
[4]MaREI, Environmental Research Institute and School of Engineering, University College Cork, Cork, Ireland

[a)]**Author to whom correspondence should be addressed:** siming.zheng@plymouth.ac.uk

ABSTRACT

Hydroelastic interaction between water waves and submerged porous elastic disks of negligible thickness in water of finite depth is investigated under the assumption of small amplitude water-wave motion and structural response. The disks are either simply supported or clamped at their edges. Wave power can be absorbed/dissipated by the disks due to their porosity. A theoretical model based on the linear potential flow theory and eigenfunction matching method is developed to solve the wave scattering problem of the submerged disks. An indirect method, employing Kochin functions, is derived based on Green's theorem to evaluate the wave power absorption/dissipation, and it produces accurate results at a lower computational cost than the conventional method. This theoretical model is applied to perform a multi-parameter study on the performance of a single submerged porous elastic disk, and an array of disks as well, particularly, in terms of near-field wave motion, disk deflection, far-field scattering coefficient, and wave power absorption/dissipation. Deploying multiple disks in an array is found to be a more promising approach for wave power absorption/dissipation compared to enlarging the area of a single disk.

Published under license by AIP Publishing. https://doi.org/10.1063/5.0006119

I. INTRODUCTION

Among a large variety of marine structures, some of them can be classified as a horizontal plate/disk, e.g., sea ice floes (Squire, 2020; Meylan and Squire, 1996) and very large floating structures, such as airports and artificial islands (Lamas-Pardo *et al.*, 2015). The horizontal dimensions of these structures are vast, while the vertical dimension is small, making it difficult to carry out experimental investigations (Zhao *et al.*, 2007). Therefore, theoretical and numerical methods have been extensively applied to study water-wave interaction of floating plates/disks.

Meylan and Squire (1996) introduced a theoretical model to reproduce the behavior of a circular flexible ice floe subjected to long-crested sea waves. Sahoo *et al.* (2001) studied the hydroelastics of a floating semi-infinite elastic plate in finite water depth. Compared to a free edge and a simply supported edge, a built-in edge was found to produce more significant wave reflection and the minimum wave transmission. Meylan *et al.* (2017) developed a theoretical model and a numerical model to study wave water scattering from a floating porous elastic disk. The conceptual model was extended recently by Zheng *et al.* (2020) to investigate a floating porous elastic plate of arbitrary shape. Oblique water-wave scattering by a floating flexible porous plate in infinite depth was studied by Koley *et al.* (2018) with the employment of a Fredholm integral equation technique. A more detailed literature review regarding the investigation of floating plates/disks can be found in Squire, 2008, 2020 and Zheng *et al.* (2020).

Submerged plates are another kind of marine structure comparable to floating plates. Compared with floating structures, the submerged plates have a reduced environmental and visual impact and are less exposed to severe wave breaking. A lower construction cost of submerged structures is another advantage (Ahmadian, 2016). The benefits of submerged structures over floating ones make them particularly attractive for protecting natural

Published under license by AIP Publishing

beaches and exploiting marine renewable energy. Indeed, extensive studies have been performed on the water-wave interaction with submerged plates.

Yu and Chwang (1993) studied the scattering of regular waves by a circular horizontal solid impermeable disk submerged at a finite depth beneath the water level by means of a theoretical model. An effect of a wave focusing around the rear of the disk was demonstrated. The wave radiation problem of a heaving submerged horizontal disk was reduced by Martin and Farina (1997) to solve a hypersingular integral equation. In their model, this equation was further reduced to one-dimensional Fredholm integral equations of the second kind. Later, Farina and Martin (1998) developed an expansion–collocation method to solve two-dimensional (2D) hypersingular integral equations for wave radiation and scattering problems of a submerged disk. Porter (2015) proposed a model based on an integral transform approach and a Galerkin method, and described the application of the model for 2D problems involving infinitely long plates and three-dimensional (3D) problems applied to circular disks. Islam *et al.* (2019) carried out a theoretical study on the interaction of water waves with a horizontal rigid disk submerged in the lower layer of a two-layer fluid. In their model, a 2D hypersingular integral equation was developed and was further reduced to a Fredholm integral equation where the unknown function depended only on a single variable. Amplification of the hydrodynamic coefficients was observed as the height of the upper layer decreased. The hypersingular integral equation-based approach was also implemented by Porter and Evans (1995) and Evans and Porter (1995) for solving water-wave interaction with vertical plates.

In the case of a submerged rigid plate/disk made from a porous medium, wave power can be dissipated due to the porosity. Assuming that the flow within the porous medium was governed by Darcy's law, Yu and Chwang (1994) examined the wave motion over a submerged porous rigid plate with the 2D boundary-element method (BEM). Moderately large values of the porosity were found to produce the maximum wave power dissipation. In order to study wave interaction with a submerged porous circular disk, Chwang and Wu (1994) developed a 3D theoretical model based on the eigenfunction matching method. In their solution, the wavenumbers, i.e., the eigenvalues of the depth-dependent eigenfunctions, above and below the porous disk were the roots of an identical complex wave dispersion relation. Later, using the Wiener–Hopf method together with the Cauchy integral method, Evans and Peter (2011) gave an analytical solution of the wave scattering for both the semi-infinite porous plate and the finite porous plate backed by a solid vertical wall. A similar method was later employed and developed by Liu and Li (2011) for wave scattering of an offshore submerged porous plate with a finite length. In their model, two techniques, i.e., (i) both horizontal and vertical eigenfunction expansions in the regions above and below the plate and (ii) symmetric and antisymmetric potentials with respect to the vertical axis, were combined; hence, finding complex roots was avoided, and simultaneously, the size for the system of truncated equations was reduced. Studies regarding the water-wave interaction with two- and multi-layer porous plates can be found by Cho *et al.* (2013) and Fang *et al.* (2017).

The problem of a submerged impermeable/porous elastic plate has also been investigated by some researchers, but not extensively. Mahmood-Ul-Hassan *et al.* (2009) presented the solutions for a submerged impermeable elastic 2D plate with semi-infinite and finite length and a 3D circular disk by using the eigenfunction matching method. The wavenumbers of the eigenfunctions above and below the elastic plate were found to be composed of two complex roots, two negative imaginary roots, and an infinite number of positive real roots of a complex wave dispersion relation. The 2D wave scattering problem of a submerged semi-infinite elastic plate was later analytically studied by Williams and Meylan (2012) using the Wiener–Hopf and residue calculus techniques, which had been used by Evans and Peter (2011) for the submerged porous rigid plate. The water-wave interaction with a submerged plate which is not only porous but also flexible is more complicated than that in the case of a submerged plate which is rigid, impermeable, or both. Cho and Kim (2000) obtained both BEM-based and analytical solutions for the hydroelastic problem of an offshore submerged porous elastic plate. In both models, the complex displacement of the plate was expanded in terms of a set of natural modes. Hence, apart from the wave diffraction problem, the radiation problems regarding these natural modes had to be solved. Behera and Sahoo (2015) solved the 2D waver scattering problem from a submerged porous elastic plate for three cases: (i) a plate in the open sea, (ii) a plate at a finite distance in front of a rigid wall, and (iii) a plate moored on a wall. In all cases, the solution was found by an eigenfunction matching method. The wavenumbers of the eigenfunctions above and below the porous elastic plate were observed to be complex. It was found that the presence of the submerged porous elastic plate caused a significant amount of wave power to be dissipated, while the waves transmitted to the lee side of the plate were dramatically weakened. More recently, Mohapatra *et al.* (2018) derived the long-wave equations under the shallow water approximation for the 2D water-wave interaction with a submerged porous elastic plate. It was shown that the wave energy dissipation was significantly dependent upon the mooring stiffness, porous-effect parameter, and position of the submerged plate.

A submerged elastic plate can be used to absorb power from water waves, provided that piezoelectric layers are bonded to both faces of the flexible substrate. The tension variations at the plate–water interface can be converted into a voltage by the piezoceramic layers owing to the piezoelectric effect, and in this way, the elastic motion excited by water waves is transformed into useful electricity. Renzi (2016) derived a hydroelectromechanical dispersion relation and analyzed the coupled hydroelectromechanical dynamics of a 2D piezoelectric plate wave energy converter (WEC). In this study, the effect of the piezoceramic power take-off (PTO) system was modeled as a complex parameter, analogous to the porous-effect parameter for porous rigid/elastic plates (e.g., Mohapatra *et al.*, 2018). Later, Buriani and Renzi (2017) extended the model to study a flexible piezoelectric WEC moored on a breakwater. The effect of plate size and its submergence on wave power absorption was not examined in their study.

In most of the above studies concerning a submerged plate, the plate was assumed to be either impermeable or rigid. Although the models developed by Renzi (2016), Behera and Sahoo (2015), and Mohapatra *et al.* (2018) *et al.* can be used to solve the wave scattering problem of a submerged porous elastic plate, they cannot be employed for the more common 3D problems, i.e., when the dimension of the plate along the wave front is not much longer than the incident wavelength. For multiple submerged

Published under license by AIP Publishing

porous elastic plates/disks deployed in an array, the hydrodynamic interaction between them will affect the wave scattering problem significantly unless they are far away from one another. To the best of the authors' knowledge, the water-wave interaction with an array of submerged porous elastic disks has not been studied.

In this paper, water-wave interaction of submerged porous elastic disks is investigated in three dimensions using a theoretical model, which is developed based on linear potential flow theory and an eigenfunction matching method. The performance of a single submerged porous elastic disk, and an array of disks as well, in terms of near-field wave motion, disk deflection, far-field scattering coefficient, and wave power absorption/dissipation is examined with the employment of the theoretical model.

The rest of this paper is organized as follows: Section II outlines the mathematical model for a wave scattering problem. Section III presents the theoretical solutions of spatial velocity potentials in the fluid domain. The methods for evaluating the scattered far-field amplitude function and wave power absorption/dissipation are given in Sec. IV. Validation of the present theoretical model is given in Sec. V. The validated model is then applied to carry out a multi-parameter study on the performance of a single submerged porous elastic disk, and an array of disks as well; the results of which can be found in Sec. VI. Finally, conclusions are drawn in Sec. VII.

II. MATHEMATICAL MODEL

An array of N submerged porous elastic disks of negligible thickness is considered. Cartesian axes are chosen with the mean free-surface coinciding with the (x, y)-plane and z measured vertically upwards. The fluid bottom is at $z = -h$, and the nth disk with a radius of R_n is placed at $z = -d_n$. N local cylindrical coordinate systems $O_n r_n \theta_n z$ for $n = 1, 2, 3, \ldots, N$ are also introduced corresponding to the nth disk. The horizontal position of O_n in the Cartesian coordinate system is (x_n, y_n). Additionally, one more cylindrical coordinate system $Or_0\theta_0 z$ is defined with its origin coinciding with the Cartesian coordinate system (not plotted in Fig. 1). $R_{n,j}$ and $\alpha_{n,j}$ denote the amplitude and the direction of the vector $\overrightarrow{O_n O_j}$, respectively.

The fluid domain is divided into two types: (I) interior regions, i.e., the regions above and below each disk, which, for the nth disk, are denoted as interior regions na and nb, respectively, and (II) exterior region, i.e., the rest extending toward infinite distance horizontally.

For the array of submerged disks subjected to undisturbed incident waves propagating in the direction β relative to the positive Ox axis with amplitude A and angular frequency ω, we assume that all amplitudes are small enough such that linear theory applies, and we make the usual assumption that the fluid is inviscid, incompressible, and irrotational. It is further assumed that all motion is time-harmonic and that the velocity potential in the fluid domain can be denoted as

$$\Phi(x, y, z, t) = \mathrm{Re}\left[\varphi(x, y, z)\mathrm{e}^{-\mathrm{i}\omega t}\right], \tag{1}$$

where φ is the time-independent complex spatial velocity potential, and it satisfies the Laplace equation; Re denotes the real part; i denotes the imaginary unit; and t is the time.

φ can be decomposed into $\varphi = \varphi_\mathrm{I} + \varphi_\mathrm{S}$, where φ_S is the scattered velocity to be determined and φ_I is the well-known velocity potential of undisturbed incident waves that can be expressed as (Zheng and Zhang, 2018; Zheng *et al.*, 2018)

$$\varphi_\mathrm{I}(x, y, z) = -\frac{\mathrm{i}gA}{\omega} Z_0(z)\mathrm{e}^{\mathrm{i}k(x\cos\beta + y\sin\beta)}, \tag{2}$$

and

$$\varphi_\mathrm{I}(r_n, \theta_n, z) = -\frac{\mathrm{i}gA}{\omega} Z_0(z)\mathrm{e}^{\mathrm{i}k(x_n\cos\beta + y_n\sin\beta)} \sum_{m=-\infty}^{\infty} \mathrm{i}^m \mathrm{e}^{-\mathrm{i}m\beta} J_m(kr_n)\mathrm{e}^{\mathrm{i}m\theta_n}, \tag{3}$$

in the general Cartesian coordinate system $Oxyz$ and the local cylindrical coordinate systems $O_n r_n \theta_n z$, respectively, where J_m denotes the Bessel function of the mth order, g is the gravitational acceleration, k denotes the wave number that satisfies $\omega^2 = gk\tanh(kh)$, and expression of $Z_0(z)$ can be found in Sec. III.

The displacement of the nth disk about $z = -d_n$ can be expressed as

$$\eta_0^{(n)}(x, y, t) = \mathrm{Re}\left[\eta_n(x, y)\mathrm{e}^{-\mathrm{i}\omega t}\right], \tag{4}$$

where η_n represents the time-independent part of the disk displacement.

The spatial velocity potential, φ, at the interface of the interior regions na and nb can be coupled to the disk displacement function, η_n, in terms of both kinematic and dynamic conditions (Meylan, 2002),

$$\partial_z\varphi = -\mathrm{i}\omega\eta_n + \mathrm{i}P_n(\varphi_- - \varphi_+) \quad \text{on} \quad r_n \in [0, R_n], z = -d_n, \tag{5}$$

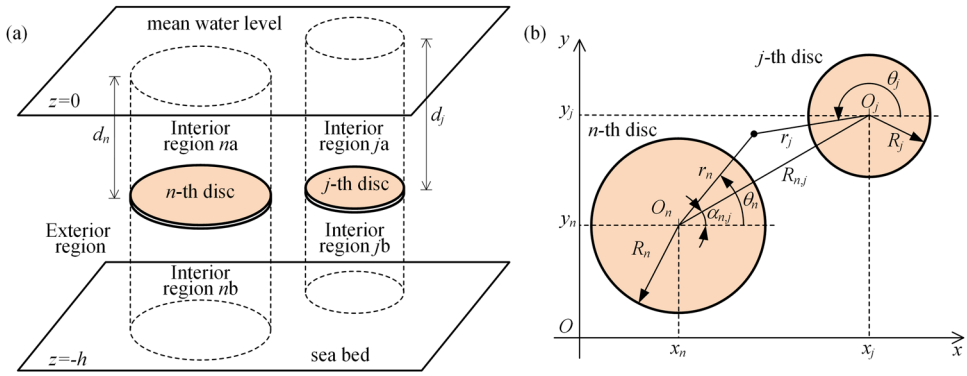


FIG. 1. Schematic of an array of submerged porous elastic disks: (a) side view and (b) plan view.

Published under license by AIP Publishing

$$g\left(\chi_n\Delta^2-\frac{\omega^2}{g}\gamma_n\right)\eta_n+\mathrm{i}\omega(\varphi_+-\varphi_-)=0 \text{ on } r_n\in[0,R_n],\ z=-d_n, \quad (6)$$

where P_n could be a complex porosity parameter of the nth disk, the real and imaginary parts of which represent the resistance and inertial effects, respectively. In this paper, for simplification, only the resistance effect is considered, i.e., P_n becomes a real porosity parameter. P_n may also be interpreted as a PTO damping coefficient, should a particular type of PTO be applied to elastic disks, which works as an array of submerged elastic wave energy converters to absorb wave power rather than to dissipate energy (e.g., Renzi, 2016). + and − denote above and below the disk, respectively; $\chi_n=\frac{D_n}{\rho g}$ and $\gamma_n=\frac{\rho_{n,\mathrm{p}}H_n}{\rho}$ denote the flexural rigidity and the mass per unit area of the disk, respectively, scaled with respect to the water density ρ, where D_n is the flexural rigidity, $\rho_{n,\mathrm{p}}$ is the nth disk density, and H_n is the thickness of the disk. Δ is the Laplacian operator in the horizontal plane.

Equations (5) and (6) can be combined into

$$\left(\chi_n\Delta^2-\frac{\omega^2}{g}\gamma_n\right)[\partial_z\varphi+\mathrm{i}P_n(\varphi_+-\varphi_-)]+\frac{\omega^2}{g}(\varphi_+-\varphi_-)=0 \quad \text{on } r_n\in[0,R_n],\ z=-d_n. \quad (7)$$

Apart from the Laplace equation and the boundary condition at the nth disk, the spatial velocity potential should satisfy the following boundary conditions:

$$\partial_z\varphi=\frac{\omega^2}{g}\varphi \text{ on } z=0, \quad (8)$$

$$\partial_z\varphi=0 \text{ on } z=-h, \quad (9)$$

$$\partial_z\varphi\big|_{z=-d_{n,+}}=\partial_z\varphi\big|_{z=-d_{n,-}} \text{ on } r_n\in[0,R_n],\quad z=-d_n. \quad (10)$$

Additionally, in the far-field horizontally, the scattered wave potential φ_S is subject to the Sommerfeld radiation condition.

The boundary conditions at the edge of each disk should be satisfied as well, which are dependent on the type of disk edge.

For submerged disks having simply supported edges, vanishing of bending moment $F_M^{(n)}$ and displacement yields

$$F_M^{(n)}=0 \text{ and } \eta_n=0 \text{ on } r_n=R_n, \quad (11)$$

where

$$F_M^{(n)}=\frac{\partial^2\eta_n}{\partial r_n^2}+\frac{\upsilon}{R_n^2}\frac{\partial^2\eta_n}{\partial\theta_n^2}+\frac{\upsilon}{R_n}\frac{\partial\eta_n}{\partial r_n}, \quad (12)$$

where υ denotes Poisson's ratio and η_n can be expressed in terms of φ by using Eq. (5).

While, in the case of submerged disks having clamped edges, both displacement and slope vanish at the edge, providing

$$\eta_n=0 \text{ and } \frac{\partial\eta_n}{\partial r_n}=0 \text{ on } r_n=R_n. \quad (13)$$

III. THEORETICAL SOLUTION TO VELOCITY POTENTIALS

The velocity potentials in the exterior region and interior regions above and below the nth disk are denoted by φ_0 and φ_n, respectively. Expressions of them are given as follows:

A. Exterior region

The eigenfunction expansion in this region is completely standard and follows the work of Zheng and Zhang (2018) and Zheng *et al.* (2018),

$$\varphi_0=\varphi_\mathrm{I}+\sum_{n=1}^{N}\sum_{m=-\infty}^{\infty}\sum_{l=0}^{\infty}A_{m,l}^{(n)}H_m(k_lr_n)Z_l(z)\mathrm{e}^{\mathrm{i}m\theta_n}, \quad (14)$$

where the accumulative term denotes the scattered wave potential, φ_S, satisfying the Sommerfeld radiation condition; $A_{m,l}^{(n)}$ are the unknown coefficients to be determined; H_m is the Hankel function of the mth order; $Z_l(z)=\frac{\cosh[k_l(z+h)]}{\cosh(k_lh)}$; $k_0=k$ and k_l for $l=1,2,3,\ldots$ are the positive real root and the infinite positive imaginary roots of the dispersion relation for the exterior region (Zheng and Zhang, 2015, 2016; and Zheng *et al.*, 2019b),

$$\omega^2=\begin{cases}gk_l\tanh(k_lh), & l=0\\ -gik_l\tan(\mathrm{i}k_lh), & l=1,2,3,\ldots.\end{cases} \quad (15)$$

With the employment of Graf's addition theorem for Bessel functions (Abramowitz and Stegun, 1964; Zheng *et al.*, 2018; and Zheng *et al.*, 2019a), Eq. (14) can be rewritten in the cylindrical coordinates $O_nr_n\theta_nz$ as

$$\begin{aligned}\varphi_0(r_n,\theta_n,z)=\varphi_\mathrm{I}&+\sum_{m=-\infty}^{\infty}\sum_{l=0}^{\infty}A_{m,l}^{(n)}H_m(k_lr_n)Z_l(z)\mathrm{e}^{\mathrm{i}m\theta_n}\\&+\sum_{\substack{j=1,\\ j\neq n}}^{N}\sum_{m=-\infty}^{\infty}\sum_{l=0}^{\infty}A_{m,l}^{(j)}Z_l(z)\\&\times\sum_{m'=-\infty}^{\infty}(-1)^{m'}H_{m-m'}(k_lR_{n,j})J_{m'}(k_lr_n)\\&\times\mathrm{e}^{\mathrm{i}(m\alpha_{j,n}-m'\alpha_{n,j})}\mathrm{e}^{\mathrm{i}m'\theta_n},\quad \text{for } r_n\le R_{n,j}.\end{aligned} \quad (16)$$

B. Interior regions

In the interior regions na and nb, the potential satisfies

$$\varphi_n(r_n,\theta_n,z)=\sum_{m=-\infty}^{\infty}\sum_{l=-2}^{\infty}B_{m,l}^{(n)}I_m(\kappa_l^{(n)}r_n)Y_l^{(n)}(z)\mathrm{e}^{\mathrm{i}m\theta_n}, \quad (17)$$

where $B_{m,l}^{(n)}$ are the unknown coefficients to be determined; I_m is the modified Bessel function of the first kind of the mth order; and

$$Y_l^{(n)}(z)=\begin{cases}-\sin(\kappa_l^{(n)}c_n)\left[\kappa_l^{(n)}h\cos(\kappa_l^{(n)}z)+\frac{\omega^2}{g}h\sin(\kappa_l^{(n)}z)\right], & z\in[-d_n,0)\\ \cos[\kappa_l^{(n)}(z+h)]\left[\kappa_l^{(n)}h\sin(\kappa_l^{(n)}d_n)+\frac{\omega^2}{g}h\cos(\kappa_l^{(n)}d_n)\right], & z\in(-h,-d_n]\end{cases} \quad (18)$$

Published under license by AIP Publishing

satisfies the free surface condition and the sea bed conditions, i.e., Eqs. (8) and (9), and also the requirement that the normal derivatives above and below the disk match, i.e., Eq. (10); $c_n = h - d_n$; $\kappa_l^{(n)}$ for $l = -2, -1, 0, 1, 2, \ldots$ are the roots of the dispersion relation for the nth submerged porous elastic disk,

$$\left(\chi_n\kappa^4 - \frac{\omega^2}{g}\gamma_n\right)\left[\kappa\sin(\kappa d_n) + \frac{\omega^2}{g}\cos(\kappa d_n)\right]\tan(\kappa c_n) = -\left[\mathrm{i}P_n\left(\chi_n\kappa^4 - \frac{\omega^2}{g}\gamma_n\right) + \frac{\omega^2}{g}\right]\left\{\left[\cos(\kappa d_n) - \frac{\omega^2}{g\kappa}\sin(\kappa d_n)\right] \times \tan(\kappa c_n) + \sin(\kappa d_n) + \frac{\omega^2}{g\kappa}\cos(\kappa d_n)\right\}, \tag{19}$$

which can be derived by applying Eq. (7) for the interior regions na and nb.

The dispersion equation can be further nondimensionalized as

$$f_n(\tilde{\kappa}) = \tilde{\kappa}(\tilde{\chi}_n\tilde{\kappa}^4 - \tilde{\alpha}\tilde{\gamma}_n)\left[\tilde{\kappa}\sin(\tilde{\kappa}\tilde{d}_n) + \tilde{\alpha}\cos(\tilde{\kappa}\tilde{d}_n)\right]\sin(\tilde{\kappa}\tilde{c}_n) + \left[\mathrm{i}\tilde{P}_n(\tilde{\chi}_n\tilde{\kappa}^4 - \tilde{\alpha}\tilde{\gamma}_n) + \tilde{\alpha}\right](\tilde{\kappa}\sin\tilde{\kappa} + \tilde{\alpha}\cos\tilde{\kappa}) = 0, \tag{20}$$

where $\tilde{\kappa} = \kappa h$, $\tilde{\chi}_n = \chi_n/h^4$, $\tilde{\gamma}_n = \gamma_n/h$, $\tilde{d} = d/h$, $\tilde{c}_n = c_n/h$, $\tilde{P}_n = P_n h$, and $\tilde{\alpha} = h\omega^2/g$.

Since the dispersion equation is even in $\tilde{\kappa}$, the solutions occur in pairs of plus and minus. With consideration of the properties of Eq. (17) and $I_m(\kappa_l^{(n)} r_n)$ regarding the sign of $\kappa_l^{(n)}$, only the roots that lie in half of the entire complex plane are required to be discussed.

When $\tilde{P} = 0$, the disk turns into an impermeable submerged elastic disk. For such circumstances, there are two positive imaginary roots, in general, such that $\tilde{\kappa}_l^{(n)} \in \mathrm{i}\mathbb{R}^+$ for $l = 0, 1$, supporting propagating waves, and an infinite number of positive real roots, $\tilde{\kappa}_l^{(n)} \in \mathbb{R}^+$ for $l = 2, 3, 4, \ldots$, corresponding to evanescent modes. Additionally, there are two complex roots, $\tilde{\kappa}_{-1}^{(n)} \in \mathbb{R}^+ + \mathrm{i}\mathbb{R}^+$ and $\tilde{\kappa}_{-2}^{(n)} = \tilde{\kappa}_{-1}^{(n)*}$ ("$*$" denotes complex-conjugate transpose, i.e., $\tilde{\kappa}_{-2}^{(n)}$ and $\tilde{\kappa}_{-1}^{(n)}$ are symmetric in the complex plane with respect to the real axis), which support damped propagating waves. For more detailed properties of the dispersion equation for the impermeable submerged elastic disk/plate, see the work of Mahmood-Ul-Hassan *et al.* (2009).

For the case with $\tilde{P} = 0$, the roots $\tilde{\kappa}_l^{(n)}$ for $l = 0, 1, 2, 3, \ldots$ are evaluated by using a bisection method, and the two complex roots $\tilde{\kappa}_{-1}^{(n)}$ and $\tilde{\kappa}_{-2}^{(n)}$ can be obtained by means of Muller's method (Press *et al.*, 2007). The roots of the dispersion relation for $\tilde{P} \neq 0$ are then derived by using the homotopy method, starting with the corresponding roots for the case of $\tilde{P} = 0$ (Meylan *et al.*, 2017).

At the interfaces between the exterior region and interior regions, the following continuity conditions of pressure and radial velocity should be satisfied:

(i) Continuity of pressure at the boundary $r_n = R_n$,

$$\varphi_0\big|_{r_n=R_n} = \varphi_n\big|_{r_n=R_n}, \quad z \in (-h, 0). \tag{21}$$

(ii) Continuity of radial velocity at the boundary $r_n = R_n$,

$$\frac{\partial\varphi_0}{\partial r_n}\bigg|_{r_n=R_n} = \frac{\partial\varphi_n}{\partial r_n}\bigg|_{r_n=R_n}, \quad z \in (-h, 0). \tag{22}$$

The type-dependent edge conditions, i.e., Eqs. (11) or (13), can be appended to the continuity conditions to close the system. A complex linear matrix equation is then derived by using the orthogonality characteristics of $Z_l(z)$ and $\mathrm{e}^{\mathrm{i}m\theta_n}$ and the eigenfunction-matching method. The unknown coefficients $A_{m,l}^{(n)}$ and $B_{m,l}^{(n)}$ can then be calculated by solving such a complex linear matrix equation. For more information about the derivation and calculation for the unknown coefficients, see Appendix A.

Once the unknown coefficients are obtained, the spatial velocity potential all over the fluid domain is known, and the response of the water surface about $z = 0$, η_0, can be calculated in a straightforward manner,

$$\eta_0(x, y, t) = \mathrm{Re}\left[\eta(x, y)\mathrm{e}^{-\mathrm{i}\omega t}\right] = \mathrm{Re}\left[\frac{\mathrm{i}\omega}{g}\varphi(x, y, 0)\mathrm{e}^{-\mathrm{i}\omega t}\right], \tag{23}$$

where η is the time-independent complex amplitude of the water elevation.

The displacement of the nth disk about $z = -d_n$ can be calculated in terms of $B_{m,l}^{(n)}$ as

$$\begin{aligned}\eta_n &= \frac{1}{\omega}\left[P_n(\varphi_- - \varphi_+) + \mathrm{i}\partial_z\varphi\right] = \frac{1}{\omega}\sum_{m=-\infty}^{\infty}\sum_{l=-2}^{\infty}B_{m,l}^{(n)}I_m\left(\kappa_l^{(n)}r_n\right) \\ &\times\left[P_n\left(\kappa_l^{(n)}h\sin(\kappa_l^{(n)}h) + \frac{\omega^2}{g}h\cos(\kappa_l^{(n)}h)\right) - \mathrm{i}\kappa_l^{(n)}\sin\left(\kappa_l^{(n)}c_n\right)\right. \\ &\left.\times\left(\kappa_l^{(n)}h\sin\left(\kappa_l^{(n)}d_n\right) + \frac{\omega^2}{g}h\cos\left(\kappa_l^{(n)}d_n\right)\right)\right]\mathrm{e}^{\mathrm{i}m\theta_n} \\ &= \frac{\mathrm{i}\omega h}{g}\sum_{m=-\infty}^{\infty}\sum_{l=-2}^{\infty}\frac{\kappa_l^{(n)}\sin\left(\kappa_l^{(n)}h\right) + \frac{\omega^2}{g}\cos\left(\kappa_l^{(n)}h\right)}{\chi_n\left(\kappa_l^{(n)}\right)^4 - \frac{\omega^2}{g}\gamma_n} \\ &\times B_{m,l}^{(n)}I_m\left(\kappa_l^{(n)}r_n\right)\mathrm{e}^{\mathrm{i}m\theta_n},\end{aligned} \tag{24}$$

where Eqs. (5) and (19) are applied.

IV. FAR-FIELD SCATTERING COEFFICIENT AND WAVE POWER ABSORPTION/DISSIPATION

A. Far-field scattering coefficient

In the fluid domain, far away from an array of porous elastic plates, only the propagating modes exist in the scattered waves. With the asymptotic forms of H_m for $r_0 \to \infty$,

$$H_m(kr_0) = \sqrt{2/\pi}\mathrm{e}^{-\mathrm{i}(m\pi/2+\pi/4)}(kr_0)^{-1/2}\mathrm{e}^{\mathrm{i}kr_0} \quad \text{for } r_0 \to \infty, \tag{25}$$

the scattered wave potential φ_S, i.e., the accumulative term in Eq. (14), can be rewritten as

$$\varphi_S = \sqrt{2/\pi}Z_0(z)\sum_{n=1}^{N}\sum_{m=-\infty}^{\infty}A_{m,0}^{(n)}\mathrm{e}^{-\mathrm{i}(m\pi/2+\pi/4)} \times (kr_n)^{-1/2}\mathrm{e}^{\mathrm{i}kr_n}\mathrm{e}^{\mathrm{i}m\theta_n}, \quad r_0 \to \infty, \tag{26}$$

which can be further expressed in the global cylindrical coordinate system $O_0r_0\theta_0z$ as

Published under license by AIP Publishing

$$\varphi_S = \sqrt{2/\pi}(kr_0)^{-1/2}e^{ikr_0}Z_0(z)\sum_{n=1}^{N}\sum_{m=-\infty}^{\infty} \times A_{m,0}^{(n)}e^{-ikR_{0,n}\cos(\alpha_{0,n}-\theta_0)}e^{-i(m\pi/2+\pi/4)}e^{im\theta_0} = A_S(\theta_0)\frac{g}{i\omega}\sqrt{2\pi}(kr_0)^{-1/2}e^{i(kr_0-\pi/4)}Z_0(z), \quad r_0 \to \infty, \quad (27)$$

where A_S is the so-called far-field scattering amplitude that is independent of r_0 and z and can be expressed as

$$A_S(\theta_0) = \frac{i\omega}{g\pi}\sum_{n=1}^{N}\sum_{m=-\infty}^{\infty}A_{m,0}^{(n)}e^{-ikR_{0,n}\cos(\alpha_{0,n}-\theta_0)}e^{im(\theta_0-\pi/2)}. \quad (28)$$

B. Wave power absorption/dissipation

1. Direct method

The energy absorbed/dissipated by the N submerged disks due to porosity, P_{diss}, can be calculated in a straightforward way,

$$P_{\text{diss}} = \frac{1}{2\rho\omega}\sum_{n=1}^{N}P_n\iint_{\Omega_n}|p|^2ds = \frac{\rho\omega}{2}\sum_{n=1}^{N}P_n\iint_{\Omega_n}|\varphi_- - \varphi_+|^2ds = \frac{\rho\omega}{2}\sum_{n=1}^{N}P_n\iint_{\Omega_n}\left|\sum_{m=-\infty}^{\infty}\sum_{l=-2}^{\infty}B_{m,l}^{(n)}I_m(\kappa_l^{(n)}r_n)e^{im\theta_n} \times\left(\kappa_l^{(n)}h\sin(\kappa_l^{(n)}h) + \frac{\omega^2}{g}h\cos(\kappa_l^{(n)}h)\right)\right|^2 ds, \quad (29)$$

where p denotes the hydrodynamic pressure loading on the disks, $p = i\omega\rho(\varphi_- - \varphi_+)$, and Ω_n represents the area occupied by the nth disk. It is noted that $P_{\text{diss}} = 0$ for $P_n = 0$ and for $P_n = \infty$ as well due to a vanishing hydrodynamic pressure and that $P_{\text{diss}} > 0$ for $0 < P_n < \infty$. Thus, there is a maximum of absorbed/dissipated power when the value of P_n is well selected.

The dimensionless quantity of P_{diss} can be defined by

$$\eta_{\text{diss}} = kP_{\text{diss}}/P_{\text{in}}, \quad (30)$$

where P_{in} is the incoming wave power per unit width of the wave front, which is given by

$$P_{\text{in}} = \frac{\rho g A^2}{2}\frac{\omega}{2k}\left(1 + \frac{2kh}{\sinh(2kh)}\right). \quad (31)$$

2. Indirect method

Apart from the straightforward way to calculate the power absorption/dissipation by the array of disks, i.e., Eq. (29), the power absorption/dissipation can also be evaluated based on the spatial potentials in the exterior region,

$$P_{\text{diss}} = \frac{\rho\omega}{4i}\iint_{\Omega_R}\left(\varphi\frac{\partial\varphi^*}{\partial r_0} - \varphi^*\frac{\partial\varphi}{\partial r_0}\right)ds, \quad (32)$$

where Ω_R represents an envisaged vertical cylindrical control surface with its radius denoted by $r_0 = R_0$, which is large enough to enclose all the disks. The derivation process of Eq. (32) can be found in Appendix B. When $r_0 = R_0 \to \infty$, Eq. (32) holds as well with the control surface Ω_R replaced by Ω_∞.

It has been derived that the integral in Eq. (32) for $r_0 \to \infty$ can be expressed in terms of Kochin functions, H_R (Falnes, 2002),

$$\iint_{\Omega_\infty}\left(\varphi\frac{\partial\varphi^*}{\partial r_0} - \varphi^*\frac{\partial\varphi}{\partial r_0}\right)ds = \frac{2iAgD(kh)}{\omega k}\text{Re}[H_R(\beta)] - \frac{iD(kh)}{2\pi k}\int_0^{2\pi}|H_R(\theta_0)|^2d\theta_0, \quad (33)$$

where H_R can be obtained from $A_{m,0}^{(n)}$ as

$$H_R(\theta_0) = 2\sum_{n=1}^{N}\sum_{m=-\infty}^{\infty}A_{m,0}^{(n)}e^{-ikR_{0,n}\cos(\alpha_{0,n}-\theta_0)}(-i)^{m+1}e^{im\theta_0} \quad (34)$$

and

$$D(kh) = \left[1 + \frac{2kh}{\sinh(2kh)}\right]\tanh(kh). \quad (35)$$

Therefore, the power absorbed/dissipated by the array of submerged porous elastic disks can be evaluated by using an indirect method based on Kochin functions,

$$P_{\text{diss}} = \frac{\rho\omega D(kh)}{k}\left(\frac{Ag}{2\omega}\text{Re}[H_R(\beta)] - \frac{1}{8\pi}\int_0^{2\pi}|H_R(\theta_0)|^2d\theta_0\right), \quad (36)$$

the result of which can be compared with that of the direct method, presenting a way to check the accuracy of the proposed theoretical model.

The straightforward method, i.e., Eq. (29), includes the surface integrals over all the disks with wave modes, including propagating, damped, and evanescent waves, all considered. As a comparison, the indirect method as given in Eq. (36) is composed of only one angular integral, regardless of the number of disks, and it produces an accurate evaluation of the wave power absorption/dissipation by merely taking the propagating waves into account, making it more promising.

Although the present theoretical model can be applied to solve the wave scattering problem from multiple submerged disks with different physical and scale parameters, Secs. V and VI are focused on identical disks; hence, $R_n = R$, $d_n = d$, $P_n = P$, $\chi_n = \chi$, and $\gamma_n = \gamma$ are employed from now on for simplification.

TABLE I. Numerical values of the complex eigenvalues $\bar{\kappa}$, i.e., solutions of the dispersion relation for the interior regions, for $\bar{\chi} = 0.01$, $\bar{\gamma} = 0.01$, $\bar{d} = 0.2$, and $\bar{\alpha} = 2.0$.

Eigenvalue	$\bar{P} = 0$	$\bar{P} = 1.0$
$\bar{\kappa}_{-2}$	2.5820 − 0.9549i	2.8663 − 0.8175i
$\bar{\kappa}_{-1}$	2.5820 + 0.9549i	2.4050 + 0.9584i
$\bar{\kappa}_0$	1.9658i	−0.0052 + 1.9660i
$\bar{\kappa}_1$	3.9996i	−0.5145 + 3.8892i
$\bar{\kappa}_2$	3.5361	3.4875 − 0.5321i
$\bar{\kappa}_3$	7.8456	7.8542 − 0.1616i
$\bar{\kappa}_4$	11.7799	11.7936 − 0.1053i
$\bar{\kappa}_5$	15.0459	15.0905 − 0.3663i
$\bar{\kappa}_6$	15.7077	15.6721 − 0.0646i
$\bar{\kappa}_7$	19.6349	19.6324 − 0.0637i
$\bar{\kappa}_8$	23.5619	23.5622 − 0.0531i
$\bar{\kappa}_9$	27.4889	27.4909 − 0.0454i
$\bar{\kappa}_{10}$	31.0947	31.1135 − 0.1704i

Published under license by AIP Publishing

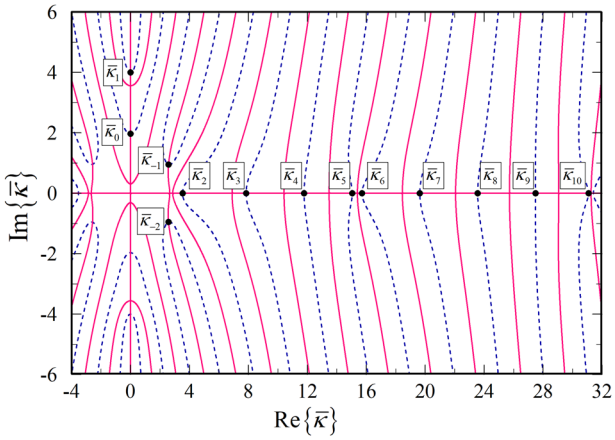


FIG. 2. Location of the first $L + 3$ eigenvalues of the dispersion relation $f(\bar{\kappa}) = 0$ in the complex $\bar{\kappa}$ plane for $L = 10$. The blue dashed lines identify the contours Re{f} = 0, whereas the pink solid lines correspond to the contours Im{f} = 0 ($\bar{\chi} = 0.01$, $\bar{\gamma} = 0.01$, $\bar{d} = 0.2$, $\bar{P} = 0$, $\bar{\alpha} = 2.0$).

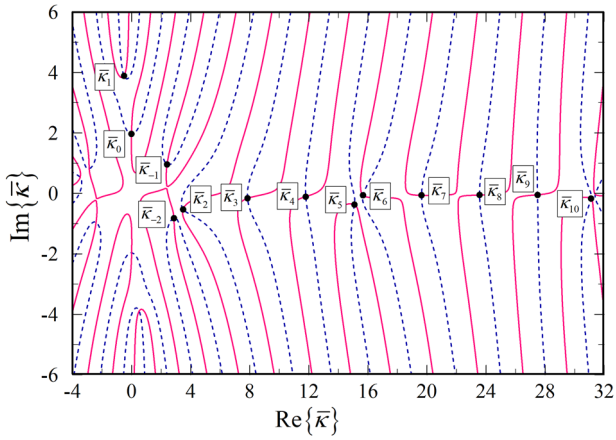


FIG. 3. As Fig. 2, but for $\bar{P} = 1.0$.

V. VALIDATION

Table I lists the first 13 roots of the dispersion relation of the interior regions calculated by the present model for the submerged impermeable/porous elastic plates with $\bar{P} = 0$ and $\bar{P} = 1.0$, and the other parameters $\bar{\chi} = 0.01$, $\bar{\gamma} = 0.01$, $\bar{d} = 0.2$, and $\bar{\alpha} = 2.0$. These roots are also plotted in Figs. 2 and 3, where the contours of Re{f} = 0 and Im{f} = 0 are illustrated as well. The roots predicted by the model are found to locate at the intersection points of the contour lines Re{f} = 0 and Im{f} = 0 exactly.

As $N = 1$, $\bar{P} = 0$ and $\bar{\chi}$ turns infinite, the case becomes wave scattering by a submerged impermeable rigid disk, which was investigated by Yu and Chwang (1993). Figure 4 illustrates the contour of the dimensionless wave amplitude above the disk. In addition to the wave amplitude contour distribution, the wave amplitudes at three specified positions P1, P2, and P3, i.e., ($r = R$, $\theta = 0$), ($r = R$, $\theta = \pi/2$) and ($r = R$, $\theta = \pi$) for the disk with different values of R are examined. Variation of the responses of the dimensionless wave amplitudes at these three points with R/λ (λ denotes wavelength) is plotted in Fig. 5, where the results with $\bar{P} \neq 0$ denoting the scattering problem of a submerged porous disk (Chwang and Wu, 1994) are also included. The present results agree very well with the published data.

Figure 6 presents the wave power absorption/dissipation by a pair of submerged porous elastic disks, which is calculated by both the direct and indirect methods. An excellent agreement between them is obtained, which, together with the results plotted in Figs. 2–5, gives confidence in the present model for solving wave scattering and predicting wave motion and wave power absorption/dissipation by submerged porous elastic disks.

VI. RESULTS AND DISCUSSION

A. Single submerged porous elastic disk

First, the performance of a single submerged porous elastic disk is investigated.

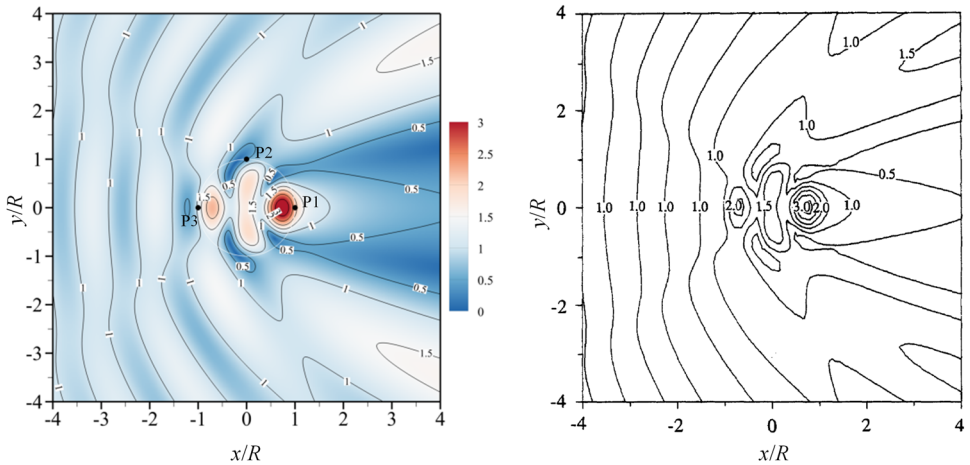


FIG. 4. Dimensionless wave amplitude distribution about a submerged rigid impermeable disk: (left) present results and (right) Yu and Chwang (1993) ($N = 1$, $x_1/h = y_1/h = 0$, $R_1/h = 1.6$, $\lambda/h = 4.0$, $\bar{\chi} = 10^3$, $\bar{\gamma} = 0.01$, $\bar{d} = 0.2$, $\beta = 0$).

Published under license by AIP Publishing

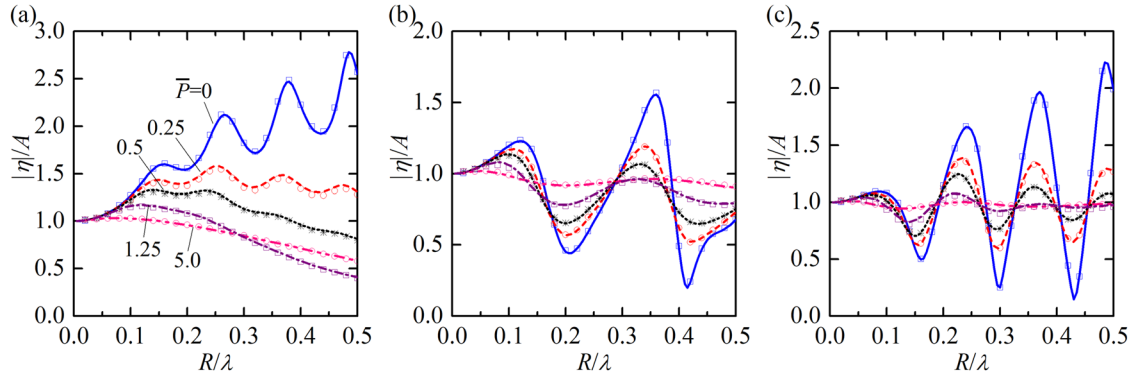


FIG. 5. Variation of dimensionless wave amplitudes at three points above the disk vs disk radius in terms of R/λ: (a) P1, (b) P2, and (c) P3 [Lines: present results; symbols: Yu and Chwang (1993) and Chwang and Wu (1994). $N = 1$, $x_1/h = y_1/h = 0$, $\lambda/h = 4.0$, $\bar{\chi} = 10^3$, $\bar{\gamma} = 0.01$, $\bar{d} = 0.2$, $\beta = 0$].

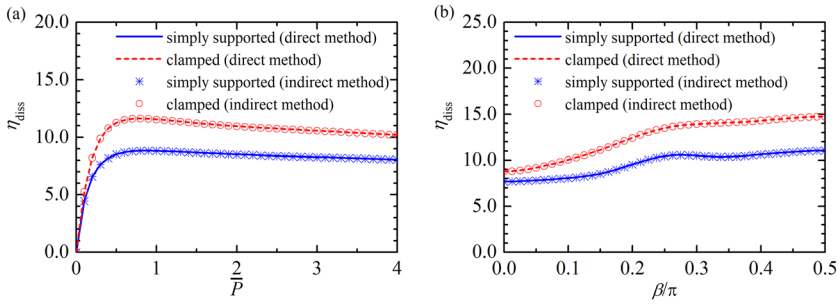


FIG. 6. Wave power absorption/dissipation of a pair of submerged disks with different kinds of edge conditions evaluated by using direct and indirect methods: (a) variation of η_{diss} with $\bar{P}$ for $\beta = \pi/6$ and (b) variation of η_{diss} with β for $\bar{P} = 1.0$ ($N = 2$, $-x_1/h = x_2/h = 2.5$, $y_1 = y_2 = 0$, $R/h = 2.0$, $\bar{\chi} = \bar{\gamma} = 0.01$, $\bar{d} = 0.2$, $\bar{\alpha} = 2.0$).

1. Effect of porosity and radius of the disk

Figure 7 presents the variation of wave power absorption/dissipation of a single submerged disk with porosity for different radii, and $\bar{\alpha} = 2.0$, $\bar{\chi} = \bar{\gamma} = 0.01$, and $\bar{d} = 0.2$. The wave power absorption/dissipation is expressed in terms of $4h^2\eta_{diss}/R^2$, which represents the averaged wave power that can be absorbed/dissipated per unit area of the disk.

For the case with $R/h = 1.0$, as expected, as $\bar{P}$ increases from 0 to 4.0, $4h^2\eta_{diss}/R^2$ first increases and then decreases after reaching the peak value around $\bar{P} = 1.0$, regardless of the edge conditions. A similar trend is observed for the other cases with larger values of R/h, while the corresponding $\bar{P}$, where the peak of $4h^2\eta_{diss}/R^2$ occurs, is smaller than 1.0, and the declining trend of the curve after reaching its peak becomes much weaker. For most of the computed range of $\bar{P}$, more wave power can be absorbed/dissipated per unit area of the disk with a smaller value of R/h.

In Fig. 8, wave power absorption/dissipation of the submerged porous elastic disk in terms of $4h^2\eta_{diss}/R^2$ is plotted against $\bar{\alpha}$ for $\bar{P} = 1.0$ and different values of R/h. When the wavelength is extremely large, i.e., $\bar{\alpha}$ and $k \to 0$, we have $4h^2\eta_{diss}/R^2 \to 0$. In the computed range of wave conditions, i.e., $\bar{\alpha} \in (0, 4.0]$, $4h^2\eta_{diss}/R^2$ increases monotonically with the increasing of $\bar{\alpha}$, regardless of the disk radius and its edge conditions. For long waves, e.g., $\bar{\alpha} < 2.0$, the disk with

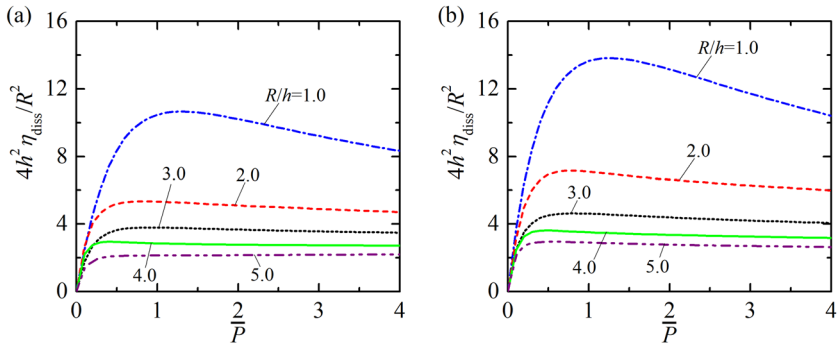


FIG. 7. Variation of wave power absorption/dissipation of a single submerged disk in terms of $4h^2\eta_{diss}/R^2$ with different porosities for different radii: (a) simply supported and (b) clamped ($N = 1$, $\bar{\alpha} = 2.0$, $\bar{\chi} = \bar{\gamma} = 0.01$, $\bar{d} = 0.2$; $M = 30$ and $L = 20$ are adopted to obtain the converged results).

Published under license by AIP Publishing

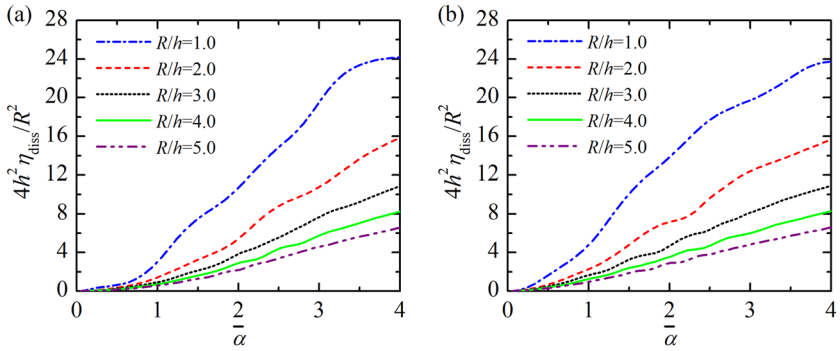


FIG. 8. Frequency response of wave power absorption in terms of $4h^2\eta_{diss}/R^2$ for a submerged porous elastic disk with different radii: (a) simply supported and (b) clamped (N = 1, $\tilde{P}$ = 1.0, $\tilde{\chi}$ = $\tilde{\gamma}$ = 0.01, $\tilde{d}$ = 0.2; M = 30 and L = 20 are adopted to obtain the converged results).

its edge clamped shows a better performance in wave power absorption/dissipation compared to that with a simply supported edge. However, for short waves, the advantage of the clamped edge is not obvious, and for some particular circumstances, e.g., R/h = 1.0 for $\bar{\alpha} \in (3.0, 4.0]$, a simply supported edge condition is even more conducive to wave power absorption/dissipation.

The contour of the near-field wave motion above a submerged impermeable/porous elastic disk with a simply supported edge condition for different radii and also the corresponding disk motion are plotted in Figs. 9 and 10.

For the impermeable disk with R/h = 1.0, there are two peaks of $|\eta|/A$ occurring right above the disk [Fig. 9(a)] in which the larger one with the peak value $|\eta|/A$ = 2.26 is located at the windward side. There are two peaks of the disk motion $|\eta_1|/A$ as well, whereas the larger peak with the peak value $|\eta_1|/A$ = 1.92 occurs at the leeward side [Fig. 10(a)]. At the leeward side of the disk in the plotted

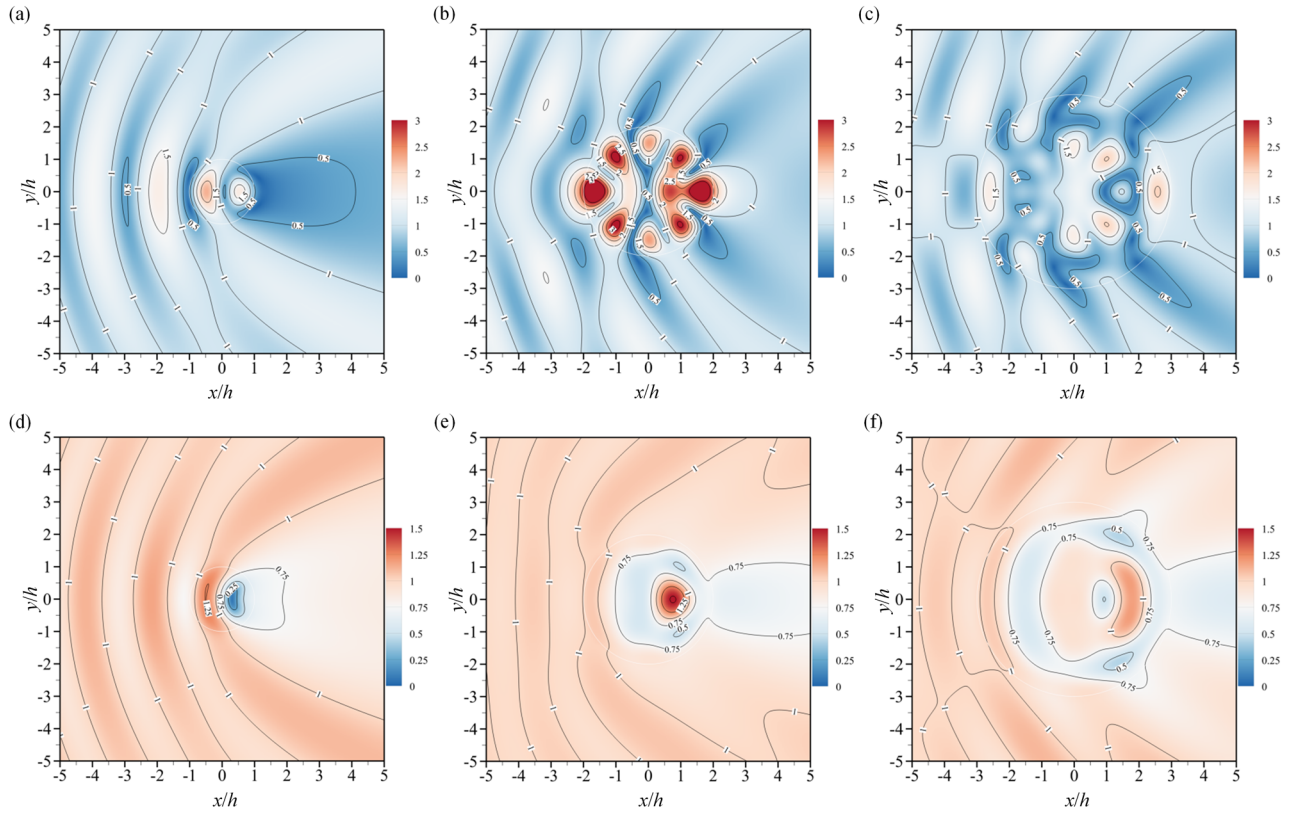


FIG. 9. Contour of the wave amplitude above a single submerged porous elastic disk $|\eta|/A$ with different values of porosity parameter and radius: (a) $\tilde{P}$ = 0, R/h = 1.0; (b) $\tilde{P}$ = 0, R/h = 2.0; (c) $\tilde{P}$ = 0, R/h = 3.0; (d) $\tilde{P}$ = 1.0, R/h = 1.0; (e) $\tilde{P}$ = 1.0, R/h = 2.0; and (f) $\tilde{P}$ = 1.0, R/h = 3.0 (N = 1, $\tilde{\alpha}$ = 2.0, β = 0, $\tilde{\chi}$ = $\tilde{\gamma}$ = 0.01, $\tilde{d}$ = 0.2, simply supported).

Published under license by AIP Publishing

domain, there is a large area where the surface waves are dramatically attenuated ($|\eta|/A < 0.5$). The regions of $|\eta|/A < 0.5$ are also found at the windward side of the disk and at the area between the two peaks of $|\eta|/A$ right above the disk as well, but with a very small area.

For the impermeable disk with $R/h = 2.0$, nine peaks of $|\eta|/A$ are observed in the interior region, in which eight are distributed along the edge of the disk, and the remaining one is located between them [Fig. 9(b)]. The most significant value of $|\eta|/A$ can be as large as 3.94, demonstrating a dramatic wave focusing effect of the submerged impermeable elastic disk. Meanwhile, there are some wave attenuation areas between the wave focusing areas as well extending outwards with $|\eta|/A < 0.5$. It is noted that at the leeward side of the disk, there is an area of the exterior region that the incident waves are amplified rather than attenuated. As shown in Fig. 10(b), there are eight peaks of the disk deflection, and the largest peak value of $|\eta_1|/A$ is 2.33.

When $R/h = 3.0$, the incident waves are attenuated at the majority of the region right above the disk [Fig. 9(c)]. At the very windward and leeward sides, and also at the central part of the interior region, the incident waves are amplified, and the largest value of $|\eta_1|/A$ is 2.05. The corresponding contour of the disk deflection, as plotted in Fig. 10(c), shows that the maximum deflection $|\eta_1|/A = 1.85$ can be obtained at $(x/h, y/h) = (1.5, 0)$.

As the submerged elastic disk changes from impermeable ($\bar{P} = 0$) into porous ($\bar{P} = 1.0$), the effect of the disk on the overall near-field wave motion is found to be clearly weakened. So is the disk deflection, as expected. Moreover, the contour shapes of both the surface wave motion and disk motion change significantly. Taking the case of $R/h = 2.0$ as an example [Figs. 9(b) and 9(e)]: as $\bar{P}$ increases from 0 to 1.0, the multiple peaks of $|\eta|/A$ disappear, and only one single peak remains with the peak value $|\eta|/A = 1.52$; at the leeward side of the disk in the exterior region, the previous wave amplification area becomes a wave attenuation area; the eight peaks of $|\eta_1|/A$ merge into three with the largest peak value 0.87.

In addition to the near-field wave motion and the corresponding disk motion of the submerged impermeable/porous elastic disk, the far-field scattering coefficients of a single submerged elastic disk with different values of the porosity parameter ($\bar{P} = 0$ and 1.0) and radius ($R/h = 1.0$, 2.0, and 3.0) for $\bar{\alpha} = 2.0$ and $\beta = 0$ are also examined (see Fig. 11). The shape of the far-field scattering coefficient curve is found to be strongly dependent on R/h. The larger the disk radius, the stronger the fluctuations of the far-field scattering coefficient curve in terms of both oscillating amplitude and

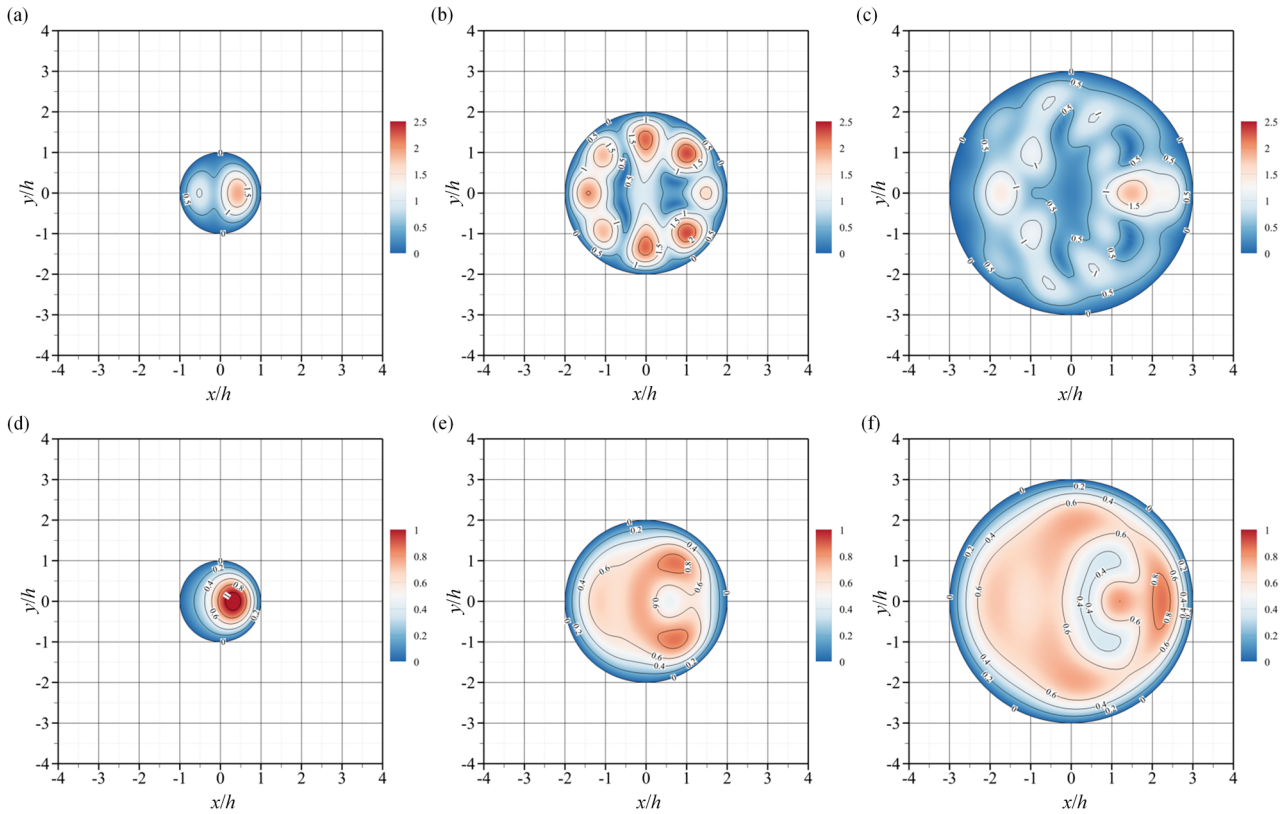


FIG. 10. Motion amplitude of the single submerged porous elastic disk $|\eta_1|/A$ with different values of porosity parameter and radius: (a) $\bar{P} = 0$, $R/h = 1.0$; (b) $\bar{P} = 0$, $R/h = 2.0$; (c) $\bar{P} = 0$, $R/h = 3.0$; (d) $\bar{P} = 1.0$, $R/h = 1.0$; (e) $\bar{P} = 1.0$, $R/h = 2.0$; and (f) $\bar{P} = 1.0$, $R/h = 3.0$ ($N = 1$, $\bar{\alpha} = 2.0$, $\beta = 0$, $\bar{\chi} = \bar{\gamma} = 0.01$, $\bar{d} = 0.2$, simply supported).

Published under license by AIP Publishing

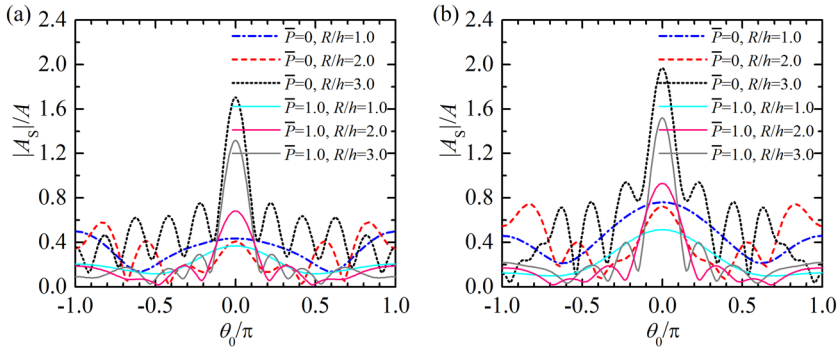


FIG. 11. Far-field scattering coefficient of a single submerged porous elastic disk with different values of porosity parameter and radius: (a) simply supported and (b) clamped (N = 1, $\bar{\alpha}$ = 2.0, β = 0, $\bar{\chi}$ = $\bar{\gamma}$ = 0.01, $\bar{d}$ = 0.2).

frequency. Additionally, the position where the largest peak value of the far-field scattering coefficient occurs is also affected by R/h. For the impermeable disk with the simply supported edge condition, the largest values of $|A_S|/A$ are observed at $\theta_0 = \pm\pi$, $\pm 0.83\pi$, and 0 for R/h = 1.0, 2.0, and 3.0, respectively. The peaks in wave reflection (Fig. 11) may be due to wave trapping by the porous disk (Sahoo *et al.*, 2000). The permeability of the disk obviously affects the phenomenon of wave trapping. Existence of the porosity reduces the overall far-field scattering coefficients, except those for some particular directions, e.g., $\theta_0 \in (-0.17\pi, 0.17\pi)$ for the disk with R/h = 2.0, simply supported edge condition; and $\theta_0 \in (-\pi, -0.9\pi) \cup (0.9\pi, \pi)$ for the disk with R/h = 3.0, clamped edge condition. For a porous elastic disk, there is a flow passing through the disk that may weaken the process of wave refraction and reflection, leading to the dissipation/absorption of the incident wave power. In the limit, as P_n tends to infinity, there would be no effect of the disk at all on wave scattering.

2. Effect of submergence of the disk

Apart from the radius of the disk, the submergence of the disk is another significant parameter affecting wave scattering by a submerged porous elastic disk.

Figure 12 plots the wave power absorption/dissipation of a single submerged disk against $\bar{P}$ for different values of d/h. It is observed that for $\bar{P} > 1.3$, the wave power absorbed/dissipated by the porous elastic disk decreases with an increase in the disk submergence. This is reasonable since the fluid motion becomes weaker and weaker with the increase in submergence, and indeed, most of the wave power is distributed at no more than a quarter wavelength below the seawater level. Interestingly, this appears to be not the case when $\bar{P} < 1.2$. In the range of $\bar{P} \in (0.3, 1.2)$, the disk with d/h = 0.15 is found to capture more wave power than the other cases examined, including the case with a smaller submergence, i.e., d/h = 0.1. This might be explained from the point of view of wave resonance. Similar to wave power extraction from a traditional heave wave energy converter (e.g., Falnes, 2002, pp. 51–52), the wave power absorbed/dissipated by an elastic disk depends not only on the wave excitation force/pressure and porosity parameter but also on the resonance condition. Compared to the case of d/h = 0.1, the wave resonance is more likely to be excited by the case of d/h = 0.15. For $\bar{P} \in (0.3, 1.2)$, the resonance condition plays a more important role than that of the wave excitation force/pressure in affecting wave power absorption/dissipation, resulting in a larger η_{diss} despite a larger submergence. This is in line with the practical requirement that the disk should remain continuously submerged and its submergence cannot be very shallow, especially for wave conditions with large amplitude or large tidal range, or both.

The corresponding near-field wave motion above the submerged porous elastic disk with different submergence values d/h = 0.1, 0.15, 0.2, 0.25, and 0.3 for $\bar{P}$ = 1.0 and the disk deflection, are given in Figs. 13 and 14, respectively. The disturbance induced by the disk on the wave motion at the exterior region is weakened with the increase in the disk submergence. Although the wave scattering is reduced as well for the majority part of the interior region, the maximum magnification of the wave amplitude increases first and then decreases, rather than decreasing monotonically

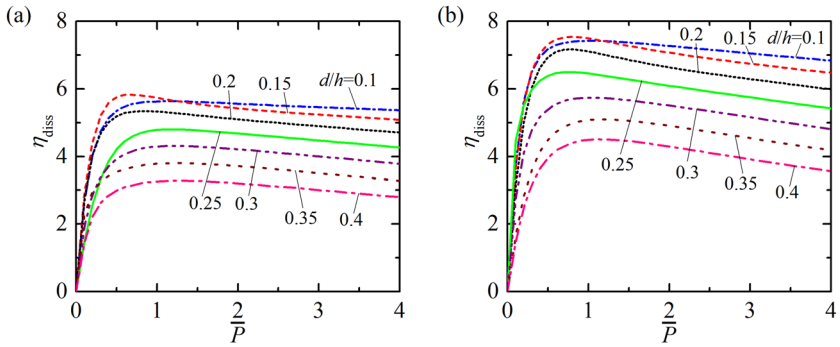


FIG. 12. Variation of wave power absorption/dissipation of a single submerged disk with different porosities for different submergence values: (a) simply supported and (b) clamped (N = 1, $\bar{\alpha}$ = 2.0, R/h = 2.0, $\bar{\chi}$ = $\bar{\gamma}$ = 0.01).

Published under license by AIP Publishing

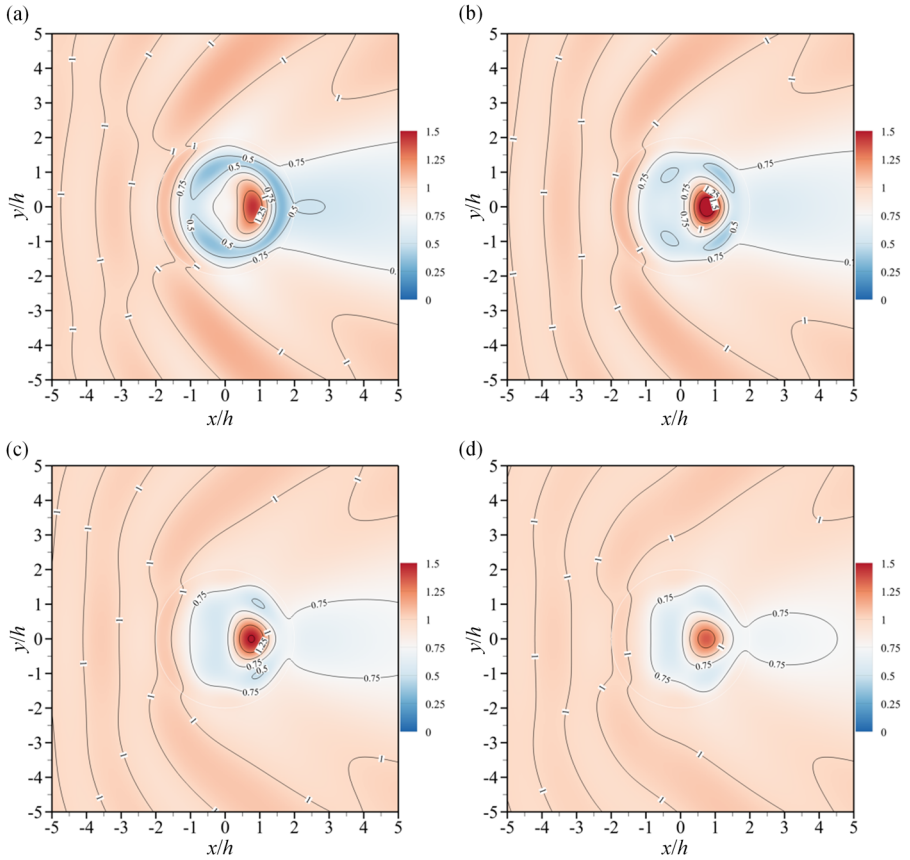


FIG. 13. Contour of the wave amplitude above a single submerged porous elastic disk $|\eta|/A$ with different submergence values: (a) d/h = 0.1, (b) d/h = 0.15, (c) d/h = 0.2, and (d) d/h = 0.25 (N = 1, $\tilde{\alpha}$ = 2.0, β = 0, $\tilde{\chi}$ = $\tilde{\gamma}$ = 0.01, R/h = 2.0, $\tilde{P}$ = 1.0, simply supported).

with the increase in the disk submergence d/h from 0.1 to 0.25. A similar trend is observed to the disk deflection via disk submergence. More specifically, the peak values of the wave amplitude and disk deformation are ($|\eta|/A$, $|\eta_1|/A$) = (1.45, 0.83), (1.65, 0.87), (1.52, 0.87), and (1.35, 0.83) for d/h = 0.1, 0.15, 0.2, and 0.25, respectively.

Figure 15 illustrates the variation of the far-field scattering coefficient against the direction for a submerged porous elastic disk with different submergence values. The far-field scattering coefficient at the very leeward side of the disk, e.g., $\theta_0 \in (-0.15\pi, 0.15\pi)$, is much larger compared to those of the remaining directions. The far-field scattering coefficient at the leeward side is found to decrease monotonously with the increase in disk submergence. For the remaining directions, there is no clear changing rule of $|A_S|/A$ vs d/h.

B. Multiple submerged porous elastic disks

In this subsection, the performance of an array of identical submerged porous elastic disks is investigated.

1. Effect of the distance between the disk centers

When the disks in an array are deployed far away from one another, the hydrodynamic interaction between them can be neglected, and each disk performs like a single disk in isolation. However, a more common circumstance is that the disks are arranged not far away but close to one another. In such a case, the hydrodynamic interaction between them may play a significant role in affecting the wave scattering problem.

Figure 16 presents the contour of wave power absorption/dissipation vs the distance between the centers of a pair of submerged porous elastic disks and the porosity parameter of the disks. It is indicated that for any specified distance between the two disks, the wave power absorption/dissipation reaches the maximum around $\tilde{P}$ = 1.0, regardless of the edge conditions. For any certain value of $\tilde{P} \in (0.5, 4]$, as $R_{1,2}/h$ increases from 5.0 to 8.0, η_{diss} first increases and then decreases after reaching the maximum. In the computed range of $\tilde{P}$ and $R_{1,2}/h$, the peak values of η_{diss} are 11.1 and 14.9 for the simply supported and clamped edge conditions, occurring at $(\tilde{P}, R_{1,2}/h)$ = (0.9, 5.26) and (0.75, 5.38), respectively.

The near-field wave motion above the pair of submerged porous elastic disks with simply supported edge condition, and the corresponding deflection of the disks with different spacing distances $R_{1,2}/h$ = 5.0, 6.0, 7.0, 8.0, $\tilde{P}$ = 1.0, $\tilde{\alpha}$ = 2.0, and β = 0 are also examined but not plotted here. In the computed domain, the largest values of $|\eta|/A$ and $|\eta_1|/A$ are (1.56, 0.88), (1.51, 0.90), (1.49, 0.87), and (1.53, 0.90) for these four cases tested, respectively.

Published under license by AIP Publishing

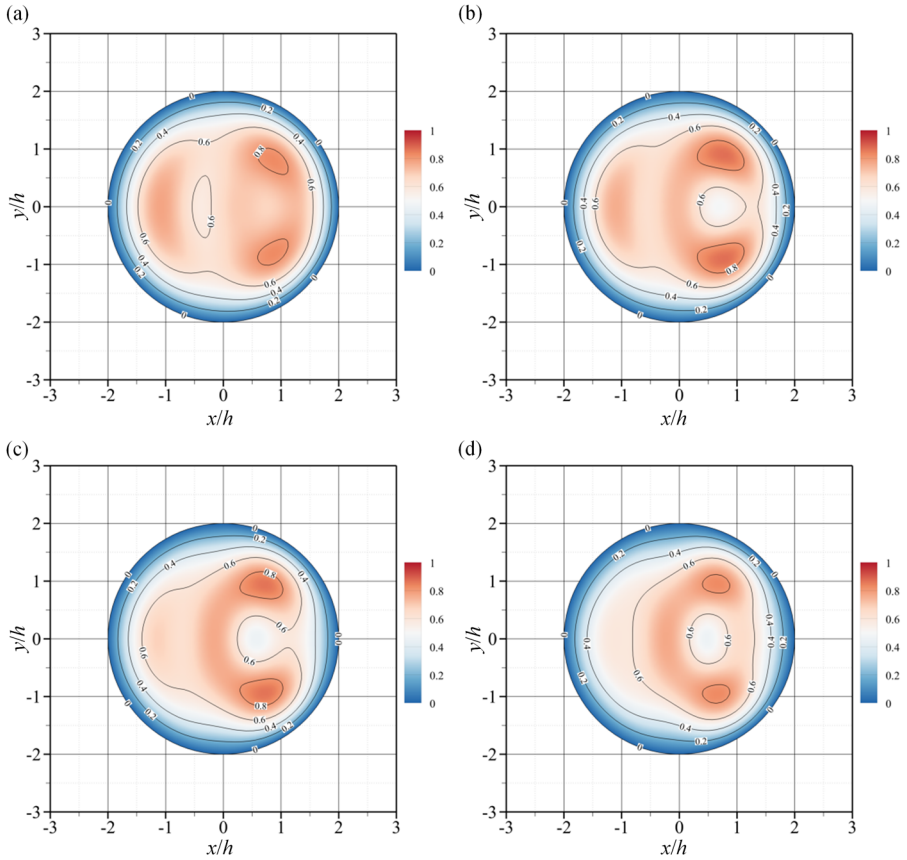


FIG. 14. Contour of the deflection of a single submerged porous elastic disk $|\eta_1|/A$ with different submergence values: (a) d/h = 0.1, (b) d/h = 0.15, (c) d/h = 0.2, and (d) d/h = 0.25 (N = 1, $\tilde{\alpha}$ = 2.0, β = 0, $\tilde{\chi} = \tilde{\gamma}$ = 0.01, R/h = 2.0, $\tilde{P}$ = 1.0, simply supported).

Figure 17 plots the far-field scattering coefficients of the pair of disks for different distances with $\tilde{P}$ = 1.0. The main peak values of $|A_S|/A$ at θ_0 = 0 remain around 1.37, and 1.87 for the simply supported and clamped edge conditions, respectively, regardless of the distance between the two submerged disks. As $R_{1,2}/h$ increases, the bandwidth of the central peak of the far-field coefficients becomes smaller. Meanwhile, the second peak, which is observed at $\theta_0/\pi \approx \pm 0.13$, turns higher and moves toward $\theta_0 = 0$.

2. Effect of the incident wave direction

Figure 18 gives the contours of the power absorption/dissipation of a pair of submerged porous elastic disks η_{diss} vs the non-dimensional porosity parameter $\tilde{P}$ and the incident wave direction β for simply supported and clamped edge conditions. It demonstrates that the maximum wave power absorption/dissipation can be achieved when the incident waves approach from the negative x-axis direction (β = 0), i.e., with the propagating direction

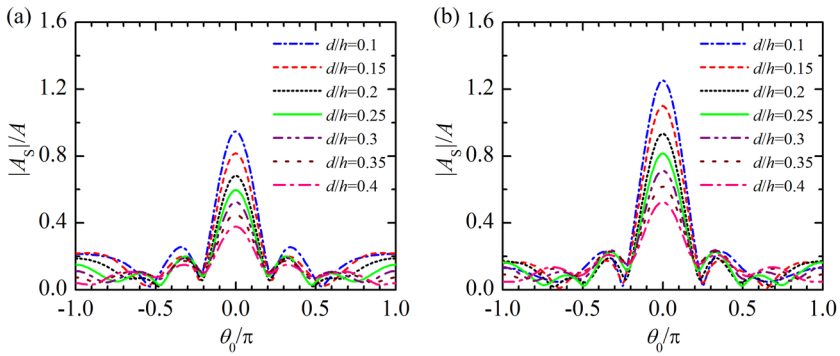


FIG. 15. Far-field scattering coefficient of a single submerged porous elastic disk with different submergence values: (a) simply supported and (b) clamped (N = 1, $\tilde{\alpha}$ = 2.0, β = 0, $\tilde{\chi} = \tilde{\gamma}$ = 0.01, R/h = 2.0, $\tilde{P}$ = 1.0).

Published under license by AIP Publishing

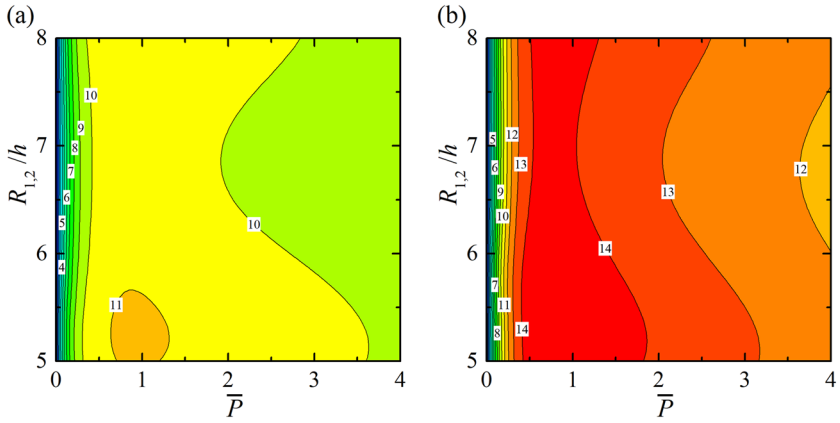


FIG. 16. Contour of wave power absorption with the distance between the disks and the porosity: (a) simply supported and (b) clamped (N = 2, $\tilde{\alpha}$ = 2.0, β = 0, $\tilde{\chi}$ = $\tilde{\gamma}$ = 0.01, R/h = 2.0, d/h = 0.2, x_1 = x_2 = 0, y_1 = $-y_2$).

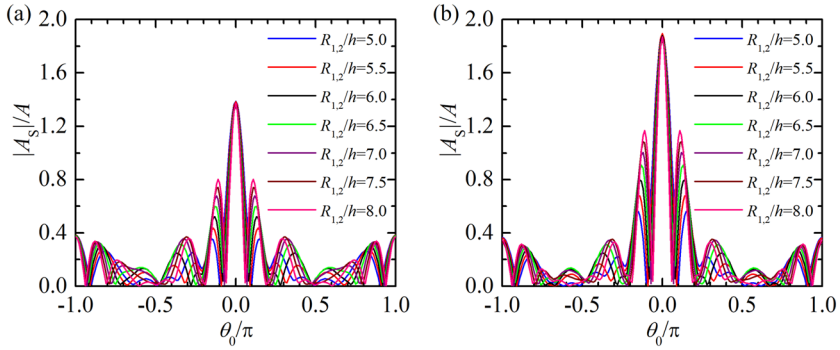


FIG. 17. Far-field scattering coefficient of a pair of submerged porous elastic disks with different distances: (a) simply supported and (b) clamped (N = 2, $\tilde{\alpha}$ = 2.0, β = 0, $\tilde{\chi}$ = $\tilde{\gamma}$ = 0.01, R/h = 2.0, d/h = 0.2, $\tilde{P}$ = 1.0).

perpendicular to the deployment line of the two disks. As the incident waves become oblique, i.e., the incident wave direction β increases from 0 toward 0.5π, less and less wave power can be generally absorbed/dissipated by the pair of disks, except a local peak of η_{diss} obtained around $\beta = 0.2\pi$ with its peak value smaller than that corresponding to $\beta = 0$. Taking the simply supported two disks with $\tilde{P}$ = 1.0 as an example, η_{diss} = 11.04, 10.37, 10.44, 8.81, and 7.68 are obtained when β = 0, $\pi/6$, $\pi/4$, $\pi/3$, and $\pi/2$, respectively, indicating a significant effect of the incident wave direction on wave power absorption/dissipation of an array of submerged porous elastic disks.

The corresponding near-field wave motion and disks' deflection of these five cases are illustrated in Figs. 19 and 20, respectively. The peak of the wave amplitude $|\eta|/A$ is observed in the area right above each disk, and specifically, it is closer to the leeward side, regardless of the incident wave direction. A shedding effect of the disk at the windward side on the wave motion above the other disk at the leeward side is demonstrated. This shedding effect becomes

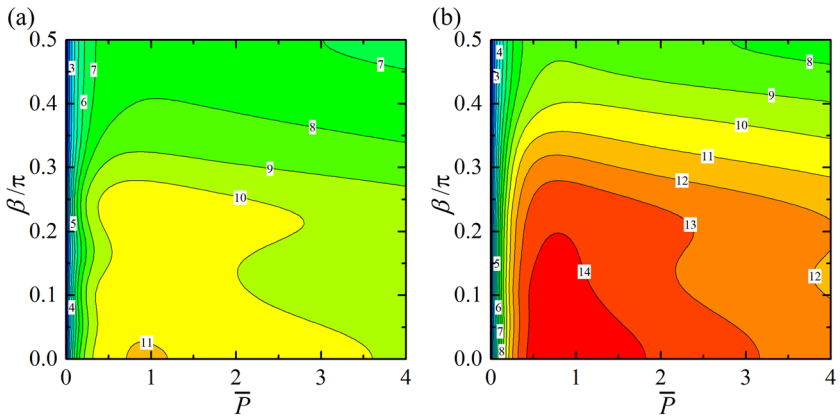


FIG. 18. Contour of wave power absorption with the incident direction and the porosity: (a) simply supported and (b) clamped (N = 2, $\tilde{\alpha}$ = 2.0, $\tilde{\chi}$ = $\tilde{\gamma}$ = 0.01, R/h = 2.0, d/h = 0.2, $R_{1,2}/h$ = 5.0, x_1 = x_2 = 0, y_1 = $-y_2$).

Published under license by AIP Publishing

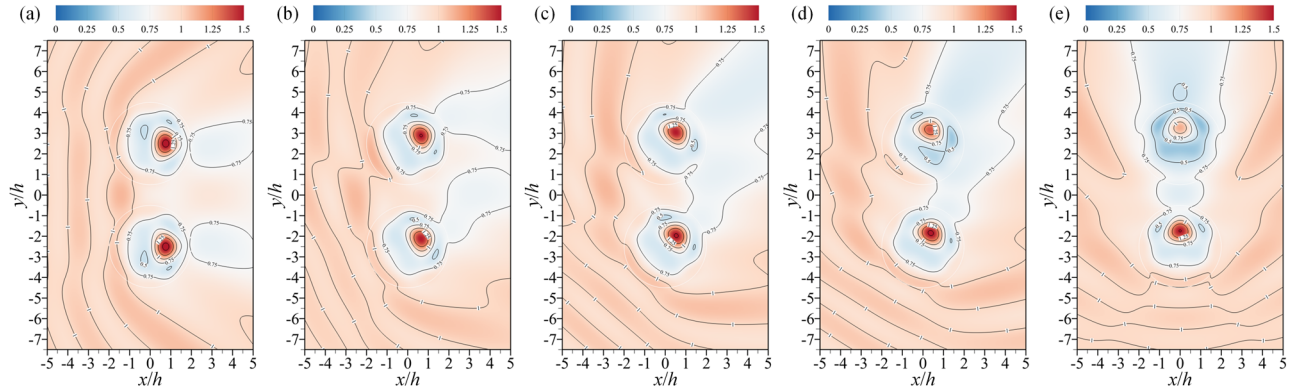


FIG. 19. Contour of the wave amplitude above a pair of submerged porous elastic disks $|\eta|/A$ with different incident wave directions: (a) $\beta = 0$, (b) $\beta = \pi/6$, (c) $\beta = \pi/4$, (d) $\beta = \pi/3$, and (e) $\beta = \pi/2$ ($N = 2$, $\tilde{\alpha} = 2.0$, $\tilde{\chi} = \tilde{\gamma} = 0.01$, $R/h = 2.0$, $d/h = 0.2$, $R_{1,2}/h = 5.0$, $x_1 = x_2 = 0$, $y_1 = -y_2$, simply supported).

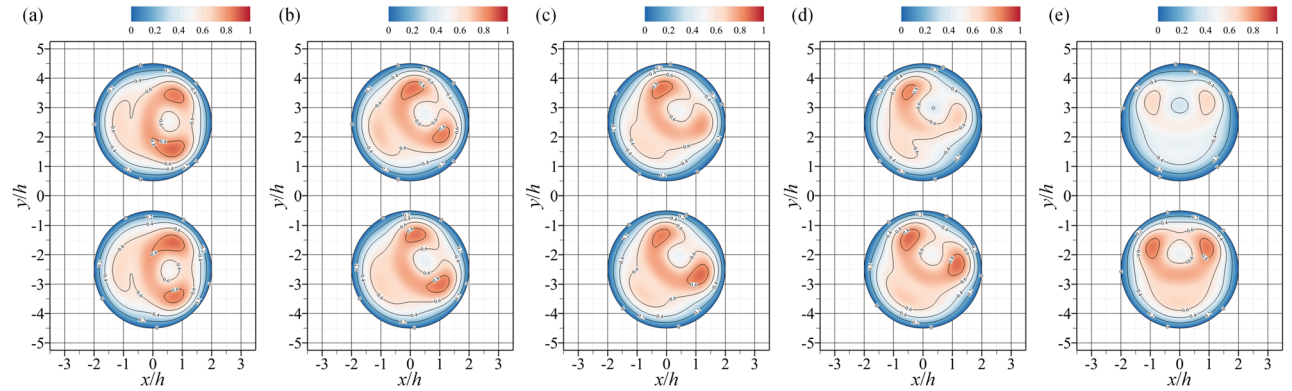


FIG. 20. Contour of the deflection of a pair of submerged porous elastic disks $|\eta_n|/A$ with different incident wave directions: (a) $\beta = 0$, (b) $\beta = \pi/6$, (c) $\beta = \pi/4$, (d) $\beta = \pi/3$, and (e) $\beta = \pi/2$ ($N = 2$, $\tilde{\alpha} = 2.0$, $\tilde{\chi} = \tilde{\gamma} = 0.01$, $R/h = 2.0$, $d/h = 0.2$, $R_{1,2}/h = 5.0$, $x_1 = x_2 = 0$, $y_1 = -y_2$, simply supported).

stronger for a larger β. The peak wave amplitude above the leeward side disk gets smaller as β increases from 0 toward $\pi/2$. It is noted that there is a wave attenuation area of $|\eta|/A < 0.75$ adjacent to the interior region and at the leeward side of each disk. In the plotted domain, with the increase in β starting from 0, these two areas of $|\eta|/A < 0.75$ adjacent to the pair of disks' interior regions become larger and move toward each other, and ultimately merge together when $\beta = \pi/4$. The shedding effect reaches the greatest at $\beta = \pi/2$ for which the peak wave amplitude of $|\eta|/A$ at the interior region of the leeward side is only 1.14, and meanwhile, a dramatic

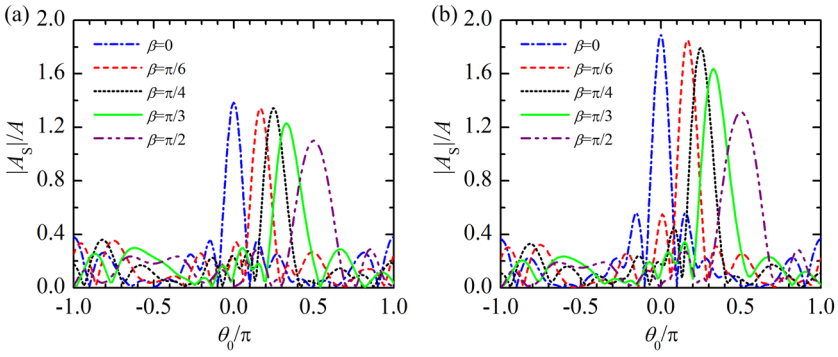


FIG. 21. Far-field scattering coefficient of a pair of submerged porous elastic disks with different incident wave directions: (a) simply supported and (b) clamped ($N = 2$, $\tilde{\alpha} = 2.0$, $\tilde{\chi} = \tilde{\gamma} = 0.01$, $R/h = 2.0$, $d/h = 0.2$, $R_{1,2}/h = 5.0$, $\tilde{P} = 1.0$).

Published under license by AIP Publishing

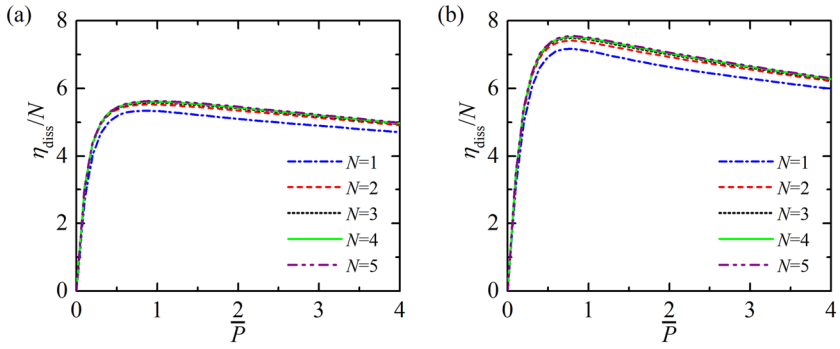


FIG. 22. Variation of wave power absorption/dissipation of an array of submerged porous elastic disks consisting of a different number of disks with different porosities: (a) simply supported and (b) clamped ($\tilde{\alpha}$ = 2.0, β = 0, R/h = 2.0, d/h = 0.2, $R_{j,j+1}/h$ = 5.0, $\tilde{\chi} = \tilde{\gamma}$ = 0.01).

large wave attenuation area of $|\eta|/A < 0.5$ appears at this interior region, and moreover, another $|\eta|/A < 0.5$ region arises at the exterior region, which is not ever observed for the remaining cases examined. The contour of the wave amplitude at the interior region of the windward side disk aligns with β, but its shape is not sensitive to the change in β. Similarly, the shedding effect on the deflection of the disks, especially the one on the leeward side, is shown in Fig. 20.

Figure 21 illustrates the far-field scattering coefficient for different incident wave directions $\beta = 0$, $\pi/6$, $\pi/4$, $\pi/3$, and $\pi/2$ with $\bar{P} = 1.0$. The direction where the main peak of $|A_S|/A$ occurs coincides with the incident wave direction, i.e., $\theta_0 = \beta$. The main peak value of $|A_S|/A$ generally decreases with the increase in β tested, except the simply supported case with $\beta = \pi/4$, the main peak value for which, by contrast, is slightly larger than that of $\beta = \pi/6$. Additionally, it is observed that the bandwidth of the main peak is enlarged as the incident waves propagate more likely in the direction along the line connecting the two disks' centers.

3. Effect of the number of disks

In order to provide a significant contribution to wave power absorption/dissipation, an array of multiple submerged, porous elastic disks should be deployed.

Figure 22 presents the variation of wave power absorption/dissipation in terms of η_{diss}/N for an array consisting of N (N = 1, 2, ..., 5) disks against $\bar{P}$ with $\tilde{\alpha}$ = 2.0, β = 0. In the computed range of $\bar{P}$, the more disks included in the array, the larger the value of η_{diss}/N, demonstrating a constructive hydrodynamic interaction for wave power absorption/dissipation. The most significant improvement of η_{diss}/N occurs when N increases from 1 to 2. For larger values of N, the increase in η_{diss}/N is weaker.

The frequency response of η_{diss}/N for the array with $\bar{P}$ = 1.0 is given in Fig. 23. For long waves, e.g., $\tilde{\alpha} < 1.5$, the curves almost overlap one another, representing a disk-number independent η_{diss}/N for these wave conditions. For the other wave conditions, especially $\tilde{\alpha} \in (2.5, 4.0]$ and $(2.0, 4.0]$ for the simply supported and clamped edge conditions, respectively, a larger value of η_{diss}/N can be obtained by the array with more disks included. Compared to enlarging the area of a single submerged porous elastic disk (see Figs. 7 and 8), deploying multiple disks in an array (Figs. 22 and 23) is demonstrated to be a more promising method for wave power absorption/dissipation.

The near-field wave motion and the disks' deflection for a different number of disks in the array are examined as well. The contours of $|\eta|/A$ at the interior regions and the $|\eta_n|/A$ are not sensitive upon the change in N. Hence, the results are not given here to save the space.

The effect of the number of disks N on the far-field scattering coefficient is also studied, the results of which are plotted in Fig. 24. The more disks included in the array, the more fluctuations of the $|A_S|/A - \theta_0$ curve observed. The values of $|A_S|/A$ at $\theta = 0$, $\pm 0.2\pi$, $\pm 0.8\pi$, and $\pm 1.0\pi$ are found to be dependent on N dramatically. Their values change proportionally with the change in N, whereas the value of $|A_S|/A$ vanishes around $\theta = \pm 0.5\pi$, regardless of the number of disks. A similar pattern was reported by Kar *et al.* (2018) in the case of wave scattering of surface gravity waves over multiple trenches and explained in terms of Bragg scattering, which is one of

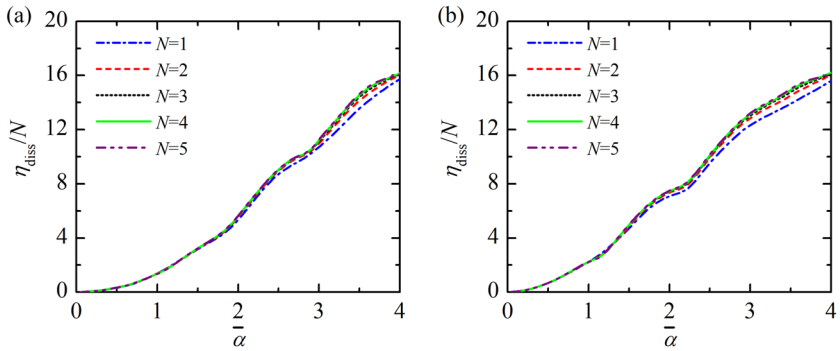


FIG. 23. Frequency response of wave power absorption/dissipation of an array of submerged porous elastic disks consisting of a different number of disks: (a) simply supported and (b) clamped ($\tilde{\alpha}$ = 2.0, β = 0, R/h = 2.0, d/h = 0.2, $R_{j,j+1}/h$ = 5.0, $\tilde{\chi} = \tilde{\gamma}$ = 0.01, $\bar{P}$ = 1.0).

Published under license by AIP Publishing

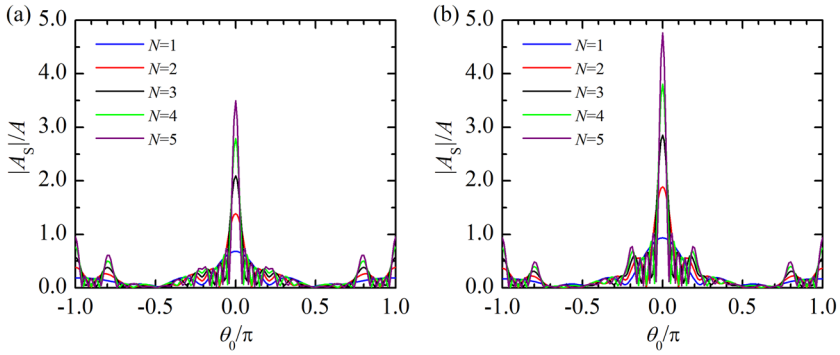


FIG. 24. Far-field scattering coefficient of an array of submerged porous elastic disks consisting of a different number of disks: (a) simply supported and (b) clamped ($N = 2$, $\tilde{\alpha} = 2.0$, $\tilde{\chi} = \tilde{\gamma} = 0.01$, $R/h = 2.0$, $d/h = 0.2$, $R_{j,j+1}/h = 5.0$, $\tilde{P} = 1.0$).

the interesting physical phenomena related to surface wave propagation over periodic sand bars/ripples or multiple floating/submerged floats (Kar *et al.*, 2019).

VII. CONCLUSIONS

A theoretical model based on linear potential flow theory and the eigenfunction matching method is developed in this paper to study the hydroelastic response of submerged porous elastic disks, which may represent a wave farm consisting of elastic plate-shaped WECs to absorb wave power or a flexible submerged elastic breakwater to attenuate ocean waves. Apart from evaluating the power absorbed/dissipated by the submerged porous elastic disks with a straightforward method, an indirect method with the employment of the Kochin functions is derived based on Green's theorem. We find that the indirect method provides a similar level of accuracy to the direct method at a fraction of the computational cost.

The proposed theoretical model was validated by comparing the present results with the published data. Both the direct and indirect methods were applied to calculate wave power absorption/dissipation of a pair of submerged elastic disks, which were found in an excellent agreement. Upon validation, the theoretical model was applied to investigate the performance of a single submerged porous elastic disk first, and then an array of disks. A multi-parameter impact analysis on wave power absorption/dissipation, near-field wave motion, disk deflection, and the far-field scattering coefficient was carried out.

The following conclusions may be drawn:

(i) For a single submerged porous elastic disk or an array of disks subjected to regular waves, there is a proper value of porosity parameter to maximize the wave power absorption/dissipation. The largest surface wave motion occurs at the region right above the submerged disks. The near-field wave motion and the disk deflection can be dramatically weakened by increasing the porosity of the disk.

(ii) Enlarging the radius of a submerged porous elastic disk generally results in less wave power that can be absorbed/dissipated per unit area of the disk. The patterns of the near-field wave motion and the disk deflection vary significantly with the change in disk radius.

(iii) For long waves, the disk with its edge clamped shows a better performance in wave power absorption/dissipation compared to that with a simply supported edge. Whereas for short waves, the advantage of the clamped edge is not obvious, and for some particular circumstances, a simply supported edge condition is even more conducive to wave power absorption/dissipation.

(iv) For a single porous elastic disk with large porosity parameter, the wave power absorbed/dissipated by the disk decreases with the increase in the disk submergence. However, for a porous elastic disk with certain values of porosity parameter, the largest wave power absorption/dissipation is obtained when the disk is submerged at a critical submergence, which is not too shallow.

(v) For a pair of submerged porous elastic disks subjected to waves propagating perpendicular to the deployment line of the disks, there is a proper distance between the disks that can maximize the wave power absorption/dissipation. The main peak of the far-field scattering coefficient remains at a certain value, regardless of the distance between the two disks. Nevertheless, the main peak bandwidth becomes smaller with the increase in the disks' distance.

(vi) When the incoming wave direction is aligned with the deployment line of the disks, the least wave power can be absorbed/dissipated because of the shedding effect of the disk at the windward side on the other one at the leeward side. The most wave power can be absorbed/dissipated when the wave incident direction is perpendicular to the deployment line of the disks.

(vii) The more disks included in an array, the larger the power that can be absorbed/dissipated per disk on average due to the constructive hydrodynamic interaction between them. The far-field scattering coefficients at some specified directions are found to be dramatically dependent on the number of disks in the array, whereas, for some of the other directions, the coefficients vanish regardless of the number of disks.

The present theoretical model is developed in the framework of potential flow theory; hence, it may not be suitable for extreme wave–structure interactions. "Bragg scattering" and "wave-trapping"/"near-trapping" effects as described by Kar *et al.*

Published under license by AIP Publishing

(2018), Sahoo *et al.* (2000), and Thompson *et al.* (2008) were not registered in our results. However, these are aspects of interest that we plan to investigate as a continuation of this line of research.

ACKNOWLEDGMENTS

This research was supported by the Intelligent Community Energy (ICE), INTERREG V FCE, European Commission (Contract No. 5025) and the Open Research Fund Program of State Key Laboratory of Hydraulic Engineering Simulation and Safety, Tianjin University (Grant No. HESS-1902).

The key data to fully reproduce the results of this work are presented in Table I.

APPENDIX A: DERIVATION PROCESS OF THE FORMULAS AND CALCULATION FOR THE UNKNOWN COEFFICIENTS $A_{m,l}^{(n)}$ AND $B_{m,l}^{(n)}$

Here, we take the case with a simply supported edge condition as an example to show how to determine the unknown coefficients $A_{m,l}^{(n)}$ and $B_{m,l}^{(n)}$. Inserting the expression of the spatial potentials for both the exterior and interior regions, i.e., Eqs. (16) and (17), into continuity conditions at the interfaces and the simply supported edge boundary conditions, Eqs. (11), (21), and (22), gives

$$
\begin{aligned}
&-\frac{\mathrm{i}gA}{\omega}Z_0(z)\mathrm{e}^{\mathrm{i}k(x_n\cos\beta+y_n\sin\beta)}\sum_{m=-\infty}^{\infty}\mathrm{i}^m\mathrm{e}^{-\mathrm{i}m\beta}J_m(kR_n)\mathrm{e}^{\mathrm{i}m\theta_n}\\
&+\sum_{m=-\infty}^{\infty}\sum_{l=0}^{\infty}A_{m,l}^{(n)}H_m(k_lR_n)Z_l(z)\mathrm{e}^{\mathrm{i}m\theta_n}+\sum_{\substack{j=1,\\ j\neq n}}^{N}\sum_{m=-\infty}^{\infty}\sum_{l=0}^{\infty}A_{m,l}^{(j)}Z_l(z)\\
&\times\sum_{m'=-\infty}^{\infty}(-1)^{m'}H_{m-m'}(k_lR_{n,j})J_{m'}(k_lR_n)\mathrm{e}^{\mathrm{i}(m\alpha_{j,n}-m'\alpha_{n,j})}\mathrm{e}^{\mathrm{i}m'\theta_n}\\
&=\sum_{m=-\infty}^{\infty}\sum_{l=-2}^{\infty}B_{m,l}^{(n)}I_m(\kappa_l^{(n)}R_n)Y_l^{(n)}(z)\mathrm{e}^{\mathrm{i}m\theta_n},\qquad -h<z<0,
\end{aligned}
\tag{A1}
$$

$$
\begin{aligned}
&-\frac{\mathrm{i}gA}{\omega}Z_0(z)\mathrm{e}^{\mathrm{i}k(x_n\cos\beta+y_n\sin\beta)}\sum_{m=-\infty}^{\infty}\mathrm{i}^m\mathrm{e}^{-\mathrm{i}m\beta}kJ_m'(kR_n)\mathrm{e}^{\mathrm{i}m\theta_n}\\
&+\sum_{m=-\infty}^{\infty}\sum_{l=0}^{\infty}A_{m,l}^{(n)}k_lH_m'(k_lR_n)Z_l(z)\mathrm{e}^{\mathrm{i}m\theta_n}\\
&+\sum_{\substack{j=1,\\ j\neq n}}^{N}\sum_{m=-\infty}^{\infty}\sum_{l=0}^{\infty}A_{m,l}^{(j)}k_lZ_l(z)\sum_{m'=-\infty}^{\infty}(-1)^{m'}H_{m-m'}(k_lR_{n,j})\\
&\times J_{m'}'(k_lR_n)\mathrm{e}^{\mathrm{i}(m\alpha_{j,n}-m'\alpha_{n,j})}\mathrm{e}^{\mathrm{i}m'\theta_n}\\
&=\sum_{m=-\infty}^{\infty}\sum_{l=-2}^{\infty}B_{m,l}^{(n)}\kappa_l^{(n)}I_m'(\kappa_l^{(n)}R_n)Y_l^{(n)}(z)\mathrm{e}^{\mathrm{i}m\theta_n},\quad -h<z<0,
\end{aligned}
\tag{A2}
$$

$$
\sum_{m=-\infty}^{\infty}\sum_{l=-2}^{\infty}\frac{\kappa_l^{(n)}\sin(\kappa_l^{(n)}h)+\frac{\omega^2}{g}\cos(\kappa_l^{(n)}h)}{\chi_n(\kappa_l^{(n)})^4-\frac{\omega^2}{g}\gamma_n}B_{m,l}^{(n)}f_M(n,m,l)\mathrm{e}^{\mathrm{i}m\theta_n}=0,
\tag{A3}
$$

$$
\sum_{m=-\infty}^{\infty}\sum_{l=-2}^{\infty}\frac{\kappa_l^{(n)}\sin(\kappa_l^{(n)}h)+\frac{\omega^2}{g}\cos(\kappa_l^{(n)}h)}{\chi_n(\kappa_l^{(n)})^4-\frac{\omega^2}{g}\gamma_n}B_{m,l}^{(n)}I_m(\kappa_l^{(n)}R_n)\mathrm{e}^{\mathrm{i}m\theta_n}=0,
\tag{A4}
$$

where

$$
\begin{aligned}
f_M(n,m,l)&=R_n^2(\kappa_l^{(n)})^2I_m''(\kappa_l^{(n)}R_n)-m^2\upsilon I_m(\kappa_l^{(n)}R_n)\\
&\quad+R_n\kappa_l\upsilon I_m'(\kappa_l^{(n)}R_n).
\end{aligned}
\tag{A5}
$$

After multiplying both sides of Eqs. (A1) and (A2) with $Z_\zeta(z)\mathrm{e}^{-\mathrm{i}\tau\theta_n}$ and integrating in $z\in[-h,0]$ and $\theta_n\in[0,2\pi]$ and using the orthogonality characteristics of them, Eqs. (A1) and (A2) can be rewritten as

$$
\begin{aligned}
&A_{\tau,\zeta}^{(n)}H_\tau(k_\zeta R_n)A_\zeta+\sum_{\substack{j=1,\\ j\neq n}}^{N}\sum_{m=-\infty}^{\infty}A_{m,\zeta}^{(j)}A_\zeta(-1)^\tau H_{m-\tau}(k_\zeta R_{n,j})\\
&\times J_\tau(k_\zeta R_n)\mathrm{e}^{\mathrm{i}(m\alpha_{j,n}-\tau\alpha_{n,j})}-\sum_{l=-2}^{\infty}B_{\tau,l}^{(n)}I_\tau(\kappa_l^{(n)}R_n)Y_{l,\zeta}^{(n)}\\
&=\frac{\mathrm{i}gA}{\omega}\delta_{0,\zeta}A_\zeta\mathrm{e}^{\mathrm{i}k(x_n\cos\beta+y_n\sin\beta)}\mathrm{i}^\tau\mathrm{e}^{-\mathrm{i}\tau\beta}J_\tau(kR_n),
\end{aligned}
\tag{A6}
$$

$$
\begin{aligned}
&A_{\tau,\zeta}^{(n)}k_\zeta H_\tau'(k_\zeta R_n)A_\zeta+\sum_{\substack{j=1,\\ j\neq n}}^{N}\sum_{m=-\infty}^{\infty}A_{m,\zeta}^{(j)}A_\zeta(-1)^\tau H_{m-\tau}(k_\zeta R_{n,j})k_\zeta\\
&\times J_\tau'(k_\zeta R_n)\mathrm{e}^{\mathrm{i}(m\alpha_{j,n}-\tau\alpha_{n,j})}-\sum_{l=-2}^{\infty}B_{\tau,l}^{(n)}\kappa_l^{(n)}I_\tau'(\kappa_l^{(n)}R_n)Y_{l,\zeta}^{(n)}\\
&=\frac{\mathrm{i}gA}{\omega}\delta_{0,\zeta}A_\zeta\mathrm{e}^{\mathrm{i}k(x_n\cos\beta+y_n\sin\beta)}\mathrm{i}^\tau\mathrm{e}^{-\mathrm{i}\tau\beta}kJ_\tau'(kR_n),
\end{aligned}
\tag{A7}
$$

where

$$
A_l=\int_{-h}^{0}Z_l^2(z)\mathrm{d}z=\frac{\sinh(k_lh)\cosh(k_lh)+k_lh}{2k_l\cosh^2(k_lh)},
\tag{A8}
$$

$$
\begin{aligned}
Y_{l,\zeta}^{(n)}&=\int_{-h}^{0}Y_l^{(n)}(z)Z_\zeta(z)\mathrm{d}z\\
&=\frac{k_\zeta h\sinh(k_\zeta c_n)\left[\frac{\omega^2}{g}\cos(\kappa_l^{(n)}h)+\kappa_l^{(n)}\sin(\kappa_l^{(n)}h)\right]}{\cosh(k_\zeta h)\left((\kappa_l^{(n)})^2+k_\zeta^2\right)}.
\end{aligned}
\tag{A9}
$$

In a similar way, after multiplying both sides of Eqs. (A3) and (A4) with $\mathrm{e}^{-\mathrm{i}\tau\theta_n}$ and integrating in $\theta_n\in[0,2\pi]$, Eqs. (A3) and (A4) can be rewritten as

$$
\sum_{l=-2}^{\infty}\frac{\kappa_l^{(n)}\sin(\kappa_l^{(n)}h)+\frac{\omega^2}{g}\cos(\kappa_l^{(n)}h)}{\chi_n(\kappa_l^{(n)})^4-\frac{\omega^2}{g}\gamma_n}B_{\tau,l}^{(n)}f_M(n,\tau,l)=0,
\tag{A10}
$$

$$
\sum_{l=-2}^{\infty}\frac{\kappa_l^{(n)}\sin(\kappa_l^{(n)}h)+\frac{\omega^2}{g}\cos(\kappa_l^{(n)}h)}{\chi_n(\kappa_l^{(n)})^4-\frac{\omega^2}{g}\gamma_n}B_{\tau,l}^{(n)}I_\tau(\kappa_l^{(n)}R_n)=0.
\tag{A11}
$$

In order to evaluate the unknown coefficients $A_{m,l}^{(n)}$ and $B_{m,l}^{(n)}$, we truncate all infinite series of vertical eigenfunctions at L, i.e., $(L+1)$ terms ($l=0,1,\ldots,L$) for $A_{m,l}^{(n)}$ and $(L+3)$ terms ($l=-2,-1,0,1,\ldots,L$) for $B_{m,l}^{(n)}$, and we take $(2M+1)$ angular terms

Published under license by AIP Publishing

($m = -M, \ldots, 0, \ldots, M$), resulting in $2N(2M + 1)(L + 2)$ unknown coefficients to be determined. After taking ($\tau = -M, \ldots, 0, \ldots, M$) and ($\zeta = 0, 1, \ldots, L$) in Eqs. (A6), (A7), (A10), and (A11), a $2N(2M + 1)(L + 2)$ order complex linear equation matrix is obtained, which can be used to determine the exact same number of unknown coefficients. M and L should be chosen to be large enough to lead to accurate results. In all the theoretical computations as given in this paper, $M = 10$ and $L = 20$ are used, unless otherwise specified.

APPENDIX B: DERIVATION PROCESS OF THE ENERGY IDENTITIES

In the fluid domain enclosed by Ω_R, the free water surface and the sea bed, but with the volume occupied by the N disks excluded, using Green's theorem (Falnes, 2002), we have

$$\oint\!\!\!\!\!\!\diint \left(\varphi\frac{\partial\varphi^*}{\partial n} - \varphi^*\frac{\partial\varphi}{\partial n}\right)\mathrm{d}s = \sum_{n=1}^{N}\iint_{\Omega_n}\left[\left(\varphi_-\frac{\partial\varphi_-^*}{\partial z} - \varphi_-^*\frac{\partial\varphi_-}{\partial z}\right) - \left(\varphi_+\frac{\partial\varphi_+^*}{\partial z} - \varphi_+^*\frac{\partial\varphi_+}{\partial z}\right)\right]\mathrm{d}s + \iint_{\Omega_R}\left(\varphi\frac{\partial\varphi^*}{\partial r} - \varphi^*\frac{\partial\varphi}{\partial r}\right)\mathrm{d}s = 0. \tag{B1}$$

With utilization of Eq. (5), Eq. (B1) can be rewritten as

$$\sum_{n=1}^{N}\iint_{\Omega_n}\left[\mathrm{i}\omega\left((\varphi_- - \varphi_+)\eta_n^* + (\varphi_-^* - \varphi_+^*)\eta_n\right) - 2\mathrm{i}P_n|\varphi_- - \varphi_+|^2\right]\mathrm{d}s = -\iint_{\Omega_R}\left(\varphi\frac{\partial\varphi^*}{\partial r} - \varphi^*\frac{\partial\varphi}{\partial r}\right)\mathrm{d}s. \tag{B2}$$

The deflection of the nth disk might be expressed by a series of modes as (Meylan *et al.*, 2017)

$$\eta_n = \sum_{q=1}^{Q} u_q^{(n)}\eta_q^{(n)}, \tag{B3}$$

where the modes $\eta_q^{(n)}$ satisfy the eigenvalue problem for the biharmonic operator,

$$\Delta^2\eta_q^{(n)} = \lambda_q\eta_q^{(n)}, \tag{B4}$$

together with the edge conditions as discussed in Sec. II; $\eta_q^{(n)}$ are orthogonal for different eigenvalues λ_q, and Q denotes the truncated numbers of infinite modes.

The dynamic motion of the disks can be coupled with the hydrodynamics by

$$\left(\mathbf{K} + \mathbf{C} - \frac{\omega^2}{g}\mathbf{M}\right)\boldsymbol{u} = \mathrm{i}\omega\rho\iint_{\Omega_{\mathrm{sum}}}(\varphi_- - \varphi_+)\boldsymbol{n}\mathrm{d}s, \tag{B5}$$

where $\Omega_{\mathrm{sum}} = \Omega_1 \cup \Omega_2 \cup \cdots \cup \Omega_N$ and $\mathbf{K}$, $\mathbf{C}$, and $\mathbf{M}$ are $(NQ) \times (NQ)$ square matrices that represent stiffness, hydrostatic-restoring, and mass matrices, respectively,

$$\mathbf{K} = \langle\chi\lambda_q\rangle_{(n-1)Q+q}; \qquad \mathbf{C} = \mathbf{I}; \qquad \mathbf{M} = \gamma\mathbf{I}, \tag{B6}$$

where $\langle c_i\rangle_j$ denotes a diagonal matrix with diagonal entries c_i at the position (j, j), $\mathbf{I}$ is the identity matrix, and

$$\boldsymbol{u} = \left[u_q^{(n)}\right]_{(n-1)Q+q}, \qquad \boldsymbol{n} = \left[\eta_q^{(n)}\right]_{(n-1)Q+q}, \tag{B7}$$

where $[c_i]_j$ represents a vector with entries c_i at the jth row.

With the employment of Eqs. (B3) and (B5), it can be proved that

$$\begin{aligned}\sum_{n=1}^{N}\iint_{\Omega_n}\left((\varphi_- - \varphi_+)\eta_n^* + (\varphi_-^* - \varphi_+^*)\eta_n\right)\mathrm{d}s &= \sum_{n=1}^{N}\iint_{\Omega_n}\left((\varphi_- - \varphi_+)\sum_{q=1}^{Q}u_q^{(n)*}\eta_q^{(n)} + (\varphi_-^* - \varphi_+^*)\sum_{q=1}^{Q}u_q^{(n)}\eta_q^{(n)}\right)\mathrm{d}s\\ &= \iint_{\Omega_{\mathrm{sum}}}\left(-(\varphi_-(\mathbf{x}) - \varphi_+(\mathbf{x}))\left[\left(\mathbf{K} + \mathbf{C} - \frac{\omega^2}{g}\mathbf{M}\right)^{-1}\mathrm{i}\omega\rho\iint_{\Omega_{\mathrm{sum}}}\left(\varphi_-^*(\bar{\mathbf{x}}) - \varphi_+^*(\bar{\mathbf{x}})\right)\boldsymbol{n}(\bar{\mathbf{x}})\mathrm{d}\bar{s}\right]^{\mathrm{T}}\boldsymbol{n}(\mathbf{x})\right.\\ &\quad\left. + \left(\varphi_-^*(\mathbf{x}) - \varphi_+^*(\mathbf{x})\right)\left[\left(\mathbf{K} + \mathbf{C} - \frac{\omega^2}{g}\mathbf{M}\right)^{-1}\mathrm{i}\omega\rho\iint_{\Omega_{\mathrm{sum}}}(\varphi_-(\bar{\mathbf{x}}) - \varphi_+(\bar{\mathbf{x}}))\boldsymbol{n}(\bar{\mathbf{x}})\mathrm{d}\bar{s}\right]^{\mathrm{T}}\boldsymbol{n}(\mathbf{x})\right)\mathrm{d}s = 0,\end{aligned} \tag{B8}$$

where we used the symmetry of the matrix $\left(\mathbf{K} + \mathbf{C} - \frac{\omega^2}{g}\mathbf{M}\right)^{-1}$ and reversed the order of integration (Flavià and Meylan, 2019).

Therefore, Eq. (B2) reads

$$\sum_{n=1}^{N}\iint_{\Omega_n}\left(-2\mathrm{i}P_n|\varphi_- - \varphi_+|^2\right)\mathrm{d}s = -\iint_{\Omega_R}\left(\varphi\frac{\partial\varphi^*}{\partial r} - \varphi^*\frac{\partial\varphi}{\partial r}\right)\mathrm{d}s, \tag{B9}$$

and hence, the power absorption/dissipation can be expressed as

$$P_{\mathrm{diss}} = \frac{\rho\omega}{2}\sum_{n=1}^{N}P_n\iint_{\Omega_n}|\varphi_- - \varphi_+|^2\mathrm{d}s = \frac{\rho\omega}{4\mathrm{i}}\iint_{\Omega_R}\left(\varphi\frac{\partial\varphi^*}{\partial r} - \varphi^*\frac{\partial\varphi}{\partial r}\right)\mathrm{d}s. \tag{B10}$$

Published under license by AIP Publishing

REFERENCES

Abramowitz, M. and Stegun, I. A., *Handbook of Mathematical Functions* (Government Printing Office, Washington, DC, 1964).

Ahmadian, A. S., "Introduction," in *Numerical Models for Submerged Breakwaters*, edited by A. S. Ahmadian (Butterworth-Heinemann, Boston, 2016), Chap. 1, pp. 1–15.

Behera, H. and Sahoo, T., "Hydroelastic analysis of gravity wave interaction with submerged horizontal flexible porous plate," J. Fluids Struct. **54**, 643–660 (2015).

Buriani, F. and Renzi, E., "Hydrodynamics of a flexible piezoelectric wave energy harvester moored on a breakwater," in *12th European Wave and Tidal Energy Conference (EWTEC)* (Cork, Ireland, 2017).

Cho, I. H. and Kim, M. H., "Interactions of horizontal porous flexible membrane with waves," J. Waterway, Port, Coastal, Ocean Eng. **126**, 245–253 (2000).

Cho, I. H., Koh, H. J., Kim, J. R., and Kim, M. H., "Wave scattering by dual submerged horizontal porous plates," Ocean Eng. **73**, 149–158 (2013).

Chwang, A. T. and Wu, J., "Wave scattering by submerged porous disk," J. Eng. Mech. **120**, 2575–2587 (1994).

Evans, D. V. and Peter, M. A., "Asymptotic reflection of linear water waves by submerged horizontal porous plates," J. Eng. Math. **69**, 135–154 (2011).

Evans, D. V. and Porter, R., "Hydrodynamic characteristics of an oscillating water column device," Appl. Ocean Res. **17**, 155–164 (1995).

Falnes, J., *Ocean Waves and Oscillating Systems: Linear Interactions Including Wave-Energy Extraction* (Cambridge University Press, 2002).

Fang, Z., Xiao, L., and Peng, T., "Generalized analytical solution to wave interaction with submerged multi-layer horizontal porous plate breakwaters," J. Eng. Math. **105**, 117–135 (2017).

Farina, L. and Martin, P., "Scattering of water waves by a submerged disc using a hypersingular integral equation," Appl. Ocean Res. **20**, 121–134 (1998).

Flavià, F. F. and Meylan, M. H., "An extension of general identities for 3d water wave diffraction with application to the diffraction transfer matrix," Appl. Ocean Res. **84**, 279–290 (2019).

Islam, N., Kundu, S., and Gayen, R., "Scattering and radiation of water waves by a submerged rigid disc in a two-layer fluid," Proc. R. Soc. A **475**, 20190331 (2019).

Kar, P., Koley, S., and Sahoo, T., "Scattering of surface gravity waves over a pair of trenches," Appl. Math. Modell. **62**, 303–320 (2018).

Kar, P., Sahoo, T., and Behera, H., "Effect of Bragg scattering due to bottom undulation on a floating dock," Wave Motion **90**, 121–138 (2019).

Koley, S., Mondal, R., and Sahoo, T., "Fredholm integral equation technique for hydroelastic analysis of a floating flexible porous plate," Eur. J. Mech. B: Fluids **67**, 291–305 (2018).

Lamas-Pardo, M., Iglesias, G., and Carral, L., "A review of very large floating structures (VLFS) for coastal and offshore uses," Ocean Eng. **109**, 677–690 (2015).

Liu, Y. and Li, Y., "An alternative analytical solution for water-wave motion over a submerged horizontal porous plate," J. Eng. Math. **69**, 385–400 (2011).

Mahmood-Ul-Hassan, H., Meylan, M. H., and Peter, M. A., "Water-wave scattering by submerged elastic plates," Q. J. Mech. Appl. Math. **62**, 321–344 (2009).

Martin, P. and Farina, L., "Radiation of water waves by a heaving submerged horizontal disc," J. Fluid Mech. **337**, 365–379 (1997).

Meylan, M. H., "Wave response of an ice floe of arbitrary geometry," J. Geophys. Res. **107**, 3005, https://doi.org/10.1029/2000jc000713 (2002).

Meylan, M. H., Bennetts, L. G., and Peter, M. A., "Water-wave scattering and energy dissipation by a floating porous elastic plate in three dimensions," Wave Motion **70**, 240–250 (2017).

Meylan, M. H. and Squire, V. A., "Response of a circular ice floe to ocean waves," J. Geophys. Res. **101**, 8869–8884, https://doi.org/10.1029/95jc03706 (1996).

Mohapatra, S. C., Sahoo, T., and Guedes Soares, C., "Surface gravity wave interaction with a submerged horizontal flexible porous plate," Appl. Ocean Res. **78**, 61–74 (2018).

Porter, R., "Linearised water wave problems involving submerged horizontal plates," Appl. Ocean Res. **50**, 91–109 (2015).

Porter, R. and Evans, D., "Complementary approximations to wave scattering by vertical barriers," J. Fluid Mech. **294**, 155–180 (1995).

Press, W. H., Teukolsky, S. A., Vetterling, W. T., and Flannery, B. P., *Numerical Recipes: The Art of Scientific Computing* (Cambridge University Press, 2007).

Renzi, E., "Hydroelectromechanical modelling of a piezoelectric wave energy converter," Proc. R. Soc. A **472**, 20160715 (2016).

Sahoo, T., Lee, M., and Chwang, A., "Trapping and generation of waves by vertical porous structures," J. Eng. Mech. **126**, 1074–1082 (2000).

Sahoo, T., Yip, T. L., and Chwang, A. T., "Scattering of surface waves by a semi-infinite floating elastic plate," Phys. Fluids **13**, 3215 (2001).

Squire, V. A., "Synergies between VLFS hydroelasticity and sea-ice research," in *The Eighteenth International Offshore and Polar Engineering Conference* (International Society of Offshore and Polar Engineers, 2008), pp. 1–13.

Squire, V. A., "Ocean wave interactions with sea ice: A reappraisal," Annu. Rev. Fluid Mech. **52**, 37–60 (2020).

Thompson, I., Linton, C., and Porter, R., "A new approximation method for scattering by long finite arrays," Q. J. Mech. Appl. Math. **61**, 333–352 (2008).

Williams, T. D. and Meylan, M. H., "The Wiener–Hopf and residue calculus solutions for a submerged semi-infinite elastic plate," J. Eng. Math. **75**, 81–106 (2012).

Yu, X. and Chwang, A. T., "Analysis of wave scattering by submerged circular disk," J. Eng. Mech. **119**, 1804–1817 (1993).

Yu, X. and Chwang, A. T., "Water waves above submerged porous plate," J. Eng. Mech. **120**, 1270–1280 (1994).

Zhao, C., Zhang, J., and Huang, W., "Vibration reduction of floating elastic plates in water waves," Marine Struct. **20**, 71–99 (2007).

Zheng, S., Antonini, A., Zhang, Y., Greaves, D., Miles, J., and Iglesias, G., "Wave power extraction from multiple oscillating water columns along a straight coast," J. Fluid Mech. **878**, 445–480 (2019a).

Zheng, S., Meylan, M. H., Fan, L., Greaves, D., and Iglesias, G., "Wave scattering by a floating porous elastic plate of arbitrary shape: A semi-analytical study," J. Fluids Struct. **92**, 102827 (2020).

Zheng, S. and Zhang, Y., "Wave diffraction from a truncated cylinder in front of a vertical wall," Ocean Eng. **104**, 329–343 (2015).

Zheng, S. and Zhang, Y., "Wave radiation from a truncated cylinder in front of a vertical wall," Ocean Eng. **111**, 602–614 (2016).

Zheng, S. and Zhang, Y., "Theoretical modelling of a new hybrid wave energy converter in regular waves," Renewable Energy **128**, 125–141 (2018).

Zheng, S., Zhang, Y., and Iglesias, G., "Wave-structure interaction in hybrid wave farms," J. Fluids Struct. **83**, 386–412 (2018).

Zheng, S., Zhang, Y., and Iglesias, G., "Coast/breakwater-integrated OWC: A theoretical model," Marine Struct. **66**, 121–135 (2019b).

Published under license by AIP Publishing